INVESTIGATION OF MICROSTRUCTURAL CHANGES IN CR9MO1 DUE TO THERMAL AGING USING SHG AND NRUS METHODS

A Thesis
Presented to
The Academic Faculty

By

Daniel Niklas Fahse

In Partial Fulfillment
of the Requirements for the Degree
Master of Science in Engineering Science and Mechanics in the
School of Civil and Environmental Engineering

Georgia Institute of Technology

December 2019

INVESTIGATION OF MICROSTRUCTURAL CHANGES IN CR9MO1 DUE TO THERMAL AGING USING SHG AND NRUS METHODS

Approved by:

Professor Laurence J. Jacobs, Advisor
School of Civil and Environmental Engineering
Georgia Institute of Technology

Dr. Jin-Yeon Kim
School of Civil and Environmental Engineering
Georgia Institute of Technology

Dr. Jianmin Qu
G.W. Woodruff School of Mechanical Engineering
Georgia Institute of Technology

Date Approved: August 22, 2019

ACKNOWLEDGEMENTS

First of all, I want to thank Professor Laurence J. Jacobs who not only acted as an adviser but also supported and motivated me throughout my studies at the Georgia Institute of Technology. Not only he gave me the opportunity to study at Georgia Tech at first place, he always helped me with any kind of problem or motivated me in personal meetings. It was always possible to have an open minded talk which led to new ideas to tackle problems.

I also would like to thank Dr. Jin-Yeon Kim for his excellent practical and professional help that always lead to new solutions and ways to push boundaries.

Thanks also to my lab mates Katie Scott, Brian Fuchs, Aurelio Bellotti, Marius Goletz and Denis Pfeifer for making the time in the lab interesting, productive and at the same time entertaining. The "Skat" breaks, a German card game, always made the hardest working day enjoyable. Special thanks goes to Marius and Denis for making this year so fun and sharing so many unforgettable moments.

I also want to thank Prof. Michael Hanss, Sibylle Langer and Dominik Hose from the University of Stuttgart for choosing me as a candidate for the exchange program and tremendous support.

Many thanks to THE SCHAUFLER FOUNDATION which partially funded this program.

Last but not least, I thank my family and all my friends in Germany for supporting me throughout my time at Georgia Tech. Especially I would like to thank Lena, who had to get along without me last year.

TABLE OF CONTENTS

LIST OF TABLES

LIST OF FIGURES

List of Symbols

Symbol	Description
σ	Stress
ε	Strain
K_0	Linear modulus
α	Hysteretic nonlinearity parameter
β	Quadratic nonlinearity parameter
δ	Cubic nonlinearity parameter
$\hat{\varepsilon}$	Local strain amplitude
$\hat{v}$	Velocity amplitude
f_0	Resonance frequency at an infinitesimal small amplitude
A_1	Amplitude of fundamental wave
A_2	Amplitude of second harmonic wave
β'	Relative quadratic nonlinearity parameter
u	Displacement
L	Length of the specimen
ρ	Mass density
F	Force
E	Young's modulus
A	Cross section of the specimen
m	Mass
a	Acceleration
c	Phase velocity
k	Wavenumber
ω	Angular frequency
n	Modenumber
Q	Squared error

R_T	Resistance at temperature T
β_{th}	Thermistor constant
V_{in}	Input voltage
V_{out}	Output voltage
E_0	Young's modulus at 0 K
$\Delta\beta$	Part of β caused by precipitates
Λ	Dislocation density
r	Average radius of the precipitates
N	Number density of the precipitates

SUMMARY

This research improves the experimental setup for non-contact nonlinear resonance ultrasound spectroscopy (NRUS) developed by Maier et al. [1] and enhances the post processing to increase the operator-independence and lower the influence of environmental changes on the measurement by modifications in the measurement procedure and the post processing.

Furthermore, the influence of ambient temperature is theoretically described. This theoretical approach is valuated on data collected with a temperature measurement added to the NRUS measurement setup. This approach could simplify the measurement procedure in the future by using the temperature measurement.

The improved measurement setup is then used to study thermal aging by measuring the non-classical hysteretic nonlinearity parameter α of the ferritic martensitic steel Cr9Mo1 at increasing thermal aging time. The results are compared to other monitoring techniques such as hardness, Young's modulus and quadratic nonlinearity parameter β. α and β show surprisingly analogous functional dependency on thermal aging.

To gain more insight about the microstructural effects and how they effect both nonlinearity parameters, the results are also compared to an in the same way monitored thermal aging process of a 17-4PH precipitate hardening stainless steel. The study is concluded with a hypothesis which can explain the observed functional dependency on aging time.

CHAPTER 1
INTRODUCTION

1.1 Motivation and Objectives

The ferritic martensitic steel Cr9Mo1 is widely used in power plants and other applications involving high temperature and high pressure applications [2]. The steel is mainly valued for its creep strength at high temperatures and relatively good corrosion resistance. Increased demand for higher power plant efficiency to reduce pollution, carbon dioxide emissions and cost of primary energy sources requires exposure to higher temperatures. The past development on 9–12% Cr steels has enabled the power plant industry to increase the steam pressure and temperature in steam power plants. This has led to an increase in efficiency from $30-35\%$ to $42-47\%$ and a carbon reduction of approximately 30% [3]. To further increase the efficiency an exposure to even higher pressures and temperatures is necessary. It is of great interest to monitor the thermal aging of critical structures in these facilities. Nondestructive evaluation (NDE) has proven to be able to assess damage and thermal aging in an early stage. The most commonly used linear ultrasonic techniques are capable of detecting macroscopic damage such as cracks or determining stiffness parameters. However, early stages of damage and material features much smaller than the wavelength of the ultrasonic wave are not detectable.

Nonlinear ultrasonic techniques have been proven to be able to detect material features below the wavelength of the ultrasonic wave by analyzing effects originated in the nonlinearity of the material. These techniques monitor for instance second harmonic generation or shift of resonance frequency.

Nonlinear resonance ultrasound spectroscopy (NRUS) quantifies the resonance

frequency shift for changing strain amplitude and has been shown to be able to monitor microstructural changes in the material [1].

The objective of this research is to further improve the measurement technique proposed by Maier et al. in [1]. This setup uses a non-contact air-coupled excitation and non-contact response measurement with a laser vibrometer. Furthermore, the environmental influences are further examined and new techniques to ensure maximum reproducibility and operator-independence are searched. This improved NRUS should then be used to monitor the thermal aging in Cr9Mo1 specimen to get a more in depth knowledge of microstructual changes and how they effect the non-classical nonlinearity parameter α.

1.2 Structure of the Thesis

After introducing the reader to the topic and the motivation behind the nonlinear techniques, chapter 2 gives a brief introduction to nonlinear elasticity and the basics of wave propagation.

The next part, chapter 3, describes the material used in this study and introduces the preliminary measurements done in other research.

Chapter 4 gives insight how the α measurements were executed and describes some improvements to obtain a higher precision.

In chapter 5 a temperature measurement, which is added to the measurement setup, is explained and the dependency of the resonance frequency to the temperature is theoretically and experimentally examined.

Chapter 6 evaluates the results of nonlinear measurement and the temperature dependency. Furthermore, the findings are compared to other research done on the precipitate hardening steel 17-4PH. Based on this interpretation, chapter 7 draws a conclusion and gives an outlook for subsequent work.

CHAPTER 2
THEORETICAL BACKGROUND

2.1 Nonlinear Elasticity

For precise description of the mechanical behavior of most solids it is necessary to assume the stress-strain relationship to be nonlinear. For many applications Hooke's Law, which assumes a linear elastic relationship between the stress σ and the strain ε with Young's Modulus E as the proportionality factor, is sufficient. The linear elastic assumption is not enough in order to explain the generation of higher harmonics upon propagation, resonance frequency shifts as well as slow dynamic effects. Thus, nonlinear terms are introduced so that the constitutive equation contains terms of different orders and a hysteretic term and is given by

$$\sigma = \int K\left(\varepsilon, \dot{\varepsilon}\right) d\varepsilon \tag{2.1}$$

with the nonlinear and hysteretic modulus

$$K\left(\varepsilon, \dot{\varepsilon}\right) = K_0 \left(1 - \beta\varepsilon - \delta\varepsilon^2 - \alpha[\hat{\varepsilon} + \varepsilon \cdot \operatorname{sign}\left(\dot{\varepsilon}\right)] + ...\right) \tag{2.2}$$

where K_0 is the linear modulus, β and δ are the quadratic and cubic classical nonlinearity parameter, α is the nonclassical hysteretic nonlinearity parameter, $\hat{\varepsilon}$ is the local strain amplitude and $\operatorname{sign}\left(\dot{\varepsilon}\right)$ is the sign function applied to the strain rate [4].

Figure 2.1 gives a schematic overview over the different contributions by each parameter by showing the linear stress-strain relationship together with the effect of each nonlinear parameter separately.

Classical nonlinearity (β and δ) mainly depends on the crystalline structure of

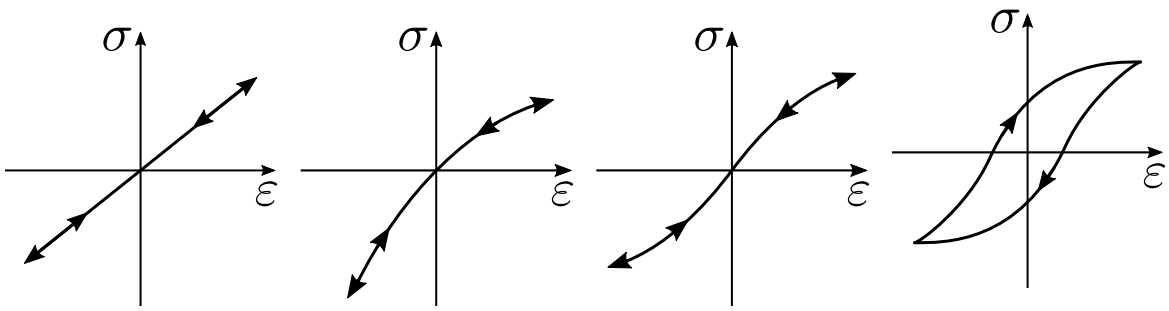

a) Linear Relationship K_0

b) Quadratic Classical Nonlinearity β

c) Cubic Classical Nonlinearity δ

d) Hysteretic Non-Classical Nonlinearity α

Figure 2.1: Overview of the nonlinearity parameters contributing to the constitutive equation. Adopted from [4].

the material and on localized strain present in the material. This strain is caused by microstructural features such as dislocations and precipitates. [5] Classical lattice nonlinearity arising from weak anharmonicity of the interatomic potential also contributes to β [6]. However, the dislocation contribution to β can greatly exceed that of the lattice anharmonicity [5]. To describe these phenomena, many theoretical models have been developed, such as dislocation pinning, dislocation dipoles, precipitates and microcracks [7].

Non-classical nonlinearity with hysteresis character and discrete memory (α) is largely observable in nonlinear mesoscopic elastic (NME) solids. Many rocks are classified in this class and the nonlinearity arises from the presence of soft defects in an elastic matrix. As opposed to classical lattice nonlinearity, this is considered as non-classical nonlinearity [6]. Experiments have shown that damaged classical elastic materials can behave as mesoscopic elastic materials [8] and damage is not only detectable on macro-defects, but even on a much smaller scale, i.e. microcracks, pores and soft bonding regions between material grain [9].

Based on the work of Preisach and Mayergoyz [10], Guyer et al. [11] developed a phenomenological model to describe the hysteretic behavior and discrete memory effect of mesoscopic-elastic materials. The model, called P-M space model, describes

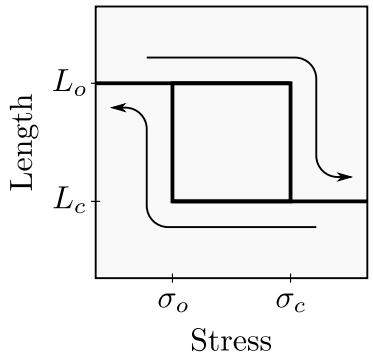

Figure 2.2: Schematic of an hysteretic element with opened length L_o, closed length L_c and according threshold stresses σ_o and σ_c. Adopted from [11].

the material as a chain of hysteretic elements. Every element is either open or closed. The behavior of one hysteretic element with opened length L_o, closed length L_c and according threshold stresses σ_o and σ_c is represented in figure 2.2. Starting with a stress lower than σ_o the element is opened and stays like this for increasing stresses until it exceeds σ_c. Above this stress the element is always closed. When the stress is lowered again, the element follows the lower path in the figure. A large number of these elements with varying L_o, L_c, σ_o and σ_c models the mesoscopic-elastic material.

To keep track of which element is opened or closed for varying stresses on the material, the "P-M space" is useful. A diagram of this representation is shown in figure 2.3. The characterizing stresses σ_o and σ_c of each element are used as coordinates in this diagram. Each element could be illustrated by a colored dot if it is opened and black dot if it is closed. When the applied stress on the material is zero all hysteresis are in the opened state and a colored triangle below the identity line appears in the diagram. All elements are in this area because σ_o has to be always smaller than σ_c.

For instance, suppose the material is taken through the stress history 0, σ_A, σ_B, $\sigma_{A'}$, σ_C, σ_D, $\sigma_{C'}$ and 0. Starting from zero stress all elements are opened. At state A all elements with $\sigma_c < \sigma_A$ are closed. All elements are in closed state at B. When the material is subsequently released to state A', the stress-strain relation follows the

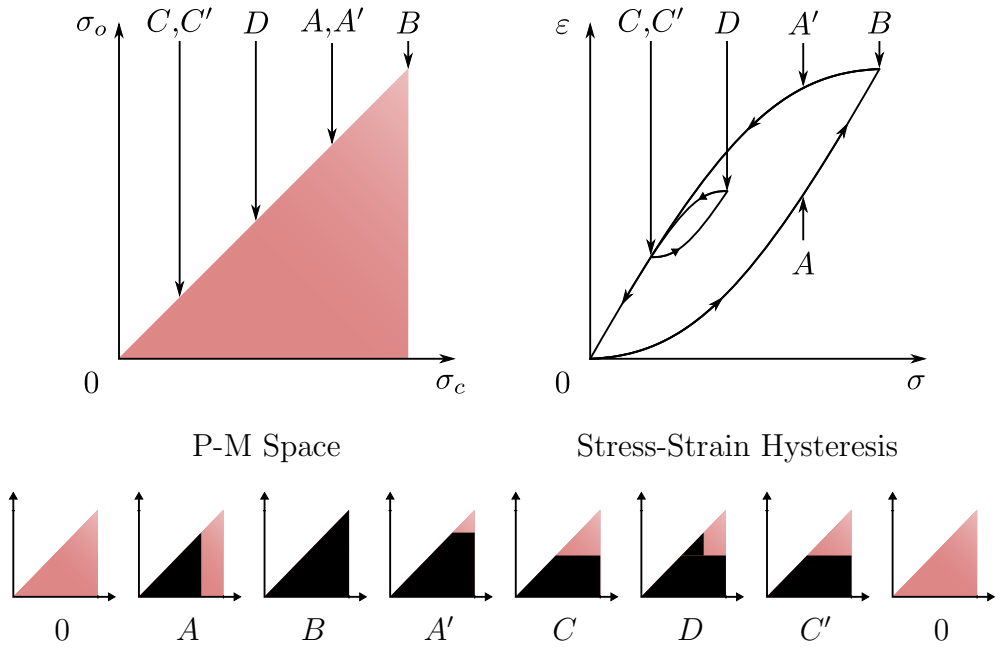

Figure 2.3: P-M space visualized for the stress history 0, σ_A, σ_B, $\sigma_{A'}$, σ_C, σ_D, $\sigma_{C'}$ and 0. The P-M space is visualized with all hysteresis elements in the opened state (top left) and for the stress history (small diagrams on the bottom). The resulting stress-strain hysteresis curve is displayed on the top right. Adopted from [11].

upper hysteresis curve. Although the stresses σ_A and $\sigma_{A'}$ are equal, the corresponding strains differ from each other. In the P-M space releasing stress is represented by horizontal lines getting colored. It becomes obvious that the material is in a different elastic state when looking at the visualizations. The P-M space reveals that a different amount of hysteretic elements are opened.

The loop C, D and C' demonstrates the phenomenon of discrete memory. Point C is only reachable when traveling this specific outer loop. Thus, it is only possible to travel the inner loop when traveling the outer loop before. Furthermore, the stress-strain trajectory of the outer loop is independent of the inner loop. The path would be the same whether or not traveling the inner loop in-between.

A quantitative theory of damping and modulus changes due to dislocations in metals is given by Granato and Lücke [12]. This model explains hysteresis of crystal materials and especially the strain-amplitude dependence of this loss. It is assumed

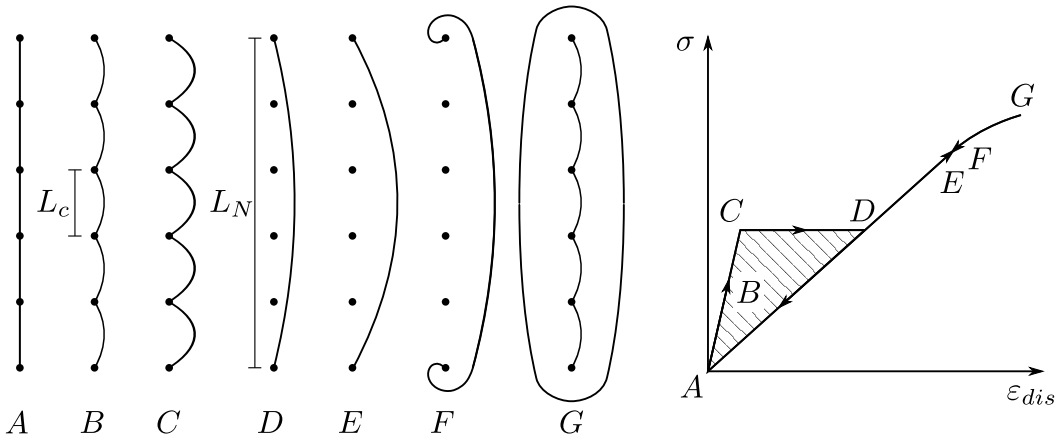

Figure 2.4: Dislocation pinning. The mechanism of dislocation pinning is visualized for increasing stress from A to G (left). The resulting stress-strain hysteresis curve with the hatched area indicating hysteretic losses is displayed on the right. Adopted from Granato and Lücke [12].

that the material contains a network of dislocations. The length of a loop is determined by the intersection of the network loops. Impurity particles in the lattice pin the loops further down. This way two characteristic lengths are established: The network length L_N and the distance L_C between the impurities. An applied external stress causes, additionally to the elastic strain, a so-called dislocation strain which is, in general, a function of frequency. However, this stress-dislocation strain law is independent of frequency in the low kilohertz range (quasi-static behavior). Qualitatively, the reaction of a dislocation line to increasing external stress is illustrated in figure 2.4. In the figure the stress is increased from left (A) to right (G). For zero applied stress the dislocation line is pinned down by the impurities on the full length L_N (A). For increasing load the loops of length L_c start to bow out (B). Until the breakaway stress is reached, the effective modulus of the stress-dislocation strain curve is determined by L_c. The dislocation line detaches from the impurity particles between steps (C) and (D). This causes a large increase of dislocation strain while the stress stays the same. After the loop is not longer pinned down by the impurities with distance L_c the characterizing length is L_N and the modulus of the stress-dislocation strain curve

is lower (D-E). Further increase in the applied stress finally leads to an irreversible detachment and formation of a closed dislocation loop (F-G). For relaxation (D-A) the path in the stress-dislocation strain graph is different and thus hysteretic losses appear (indicated by the hatched area in figure 2.4). For the whole decrease in stress the network length L_N determines the modulus and the dislocation line is not pinned to the impurities until A. Thus, the loss is proportional to the enclosed area of the hysteresis loop. Granato and Lücke further describe a frequency dependent dynamic loss which is due to a phase lag of the oscillating stress. Therefore, this loss is clearly frequency dependent since it has a resonance type character. It is largest close to the resonance frequency, determined by the loop length, and disappearing for low and high frequencies.

2.1.1 Resonance Ultrasound Spectroscopy (RUS)

Resonance Ultrasound Spectroscopy (RUS) is a linear ultrasonic technique to extract the elastic constants of a sample with known geometry, density and resonance frequencies. High accuracy can be achieved as long as the geometry is well defined and the material is homogeneous [13]. In this work thin bar specimens are used and longitudinal vibration modes are considered. Thus, only the one-dimensional Young's modulus E can be acquired.

2.1.2 Nonlinear Resonance Ultrasound Spectroscopy (NRUS)

Nonlinear Elastic Wave Spectrocopy (NEWS) embodies a wide range of methods to examine damage in materials. These methods are based on the effects caused by material nonlinearity such as distortion, generation of harmonics or frequency shift over driving amplitude in resonance conditions [8]. Nonlinear Resonance Ultrasound Spectroscopy (NRUS) is a subset of NEWS and measures the change of resonance frequency as a function of amplitude and can consequently be understood as an exten-

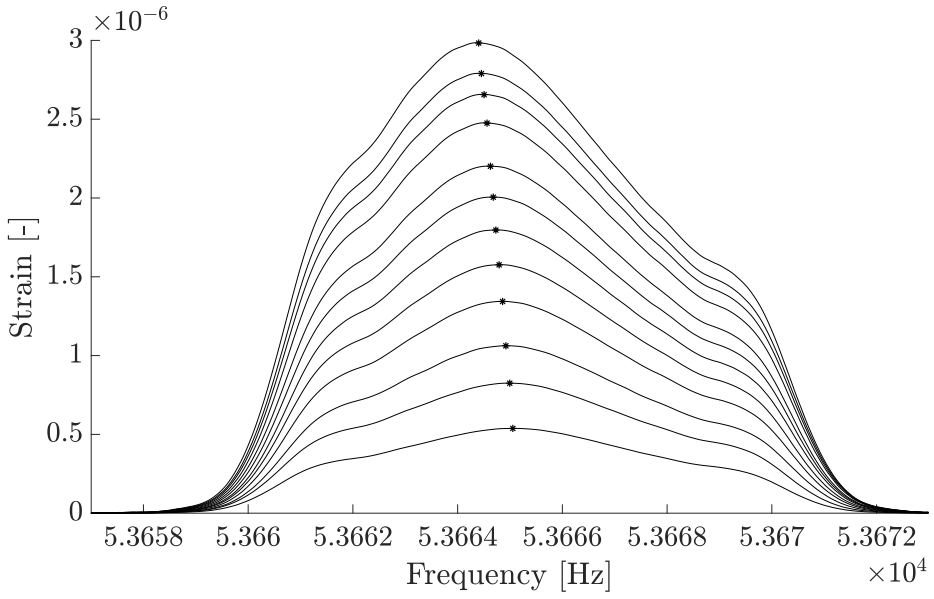

Figure 2.5: Typical resonance response of a material with nonclassical hysteretic nonlinearity. The dots indicate the maximum of every curve. A shift to lower frequencies at higher excitation amplitudes is visible.

sion of the linear RUS method. Figure 2.5 shows a typical response of a nonclassical hysteretic material for increasing excitation amplitudes. The shift to lower frequencies indicates a material softening for higher amplitudes. The hysteretic nonlinearity parameter α is derived as

$$\frac{\Delta f}{f_0} = \alpha \hat{\varepsilon}, \tag{2.3}$$

with the resonance frequency at an infinitesimal small amplitude f_0, the shift of resonance frequency Δf and the strain amplitude $\hat{\varepsilon}$.

In previous research the NRUS method was applied to a wide range of materials, including rocks, composites, bones and metals. The material is generally excited with impact hammers [14], electromagnetic acoustic transducers [15], loudspeakers [8], piezo-electric transducers [16] or in recent research also with electromagnetic excitation [17]. To receive the signal contact-based piezo-electric transducers, accelerometers or noncontact detection with laser vibrometers are commonly used.

2.1.3 Second Harmonic Generation

Second harmonic generation (SHG) is a method which has been shown to be able to detect microstructural changes in metals [5]. When a monochromatic wave is propagating through a nonlinear elastic material the interaction with microstructural features generates higher harmonic waves. Thus, waves are formed with frequencies which are an integer multiple of the initial frequency. This effect is quantified with the classical quadratic nonlinearity parameter β. The second harmonic amplitude A_2 can be related to the first harmonic amplitude A_1 with the the classical quadratic nonlinearity parameter β according to

$$\beta = \frac{A_2}{A_1^2}\left(\frac{8}{\kappa^2 x}\right) \tag{2.4}$$

where κ is the wavenumber and x is the propagated distance. Thus, $\beta \cdot \frac{\kappa^2}{8}$ acts as the proportionality factor between the fraction of the second harmonics amplitude and the square of the first harmonics amplitude and the propagation distance x:

$$x \propto \frac{A_2}{A_1^2} \tag{2.5}$$

Because only electrical amplitudes are measured and effects of the experimental setup are not considered only the relative classical quadratic nonlinearity parameter β', defined by

$$\beta \propto \beta' = \frac{A_2}{A_1^2 x} \tag{2.6}$$

is acquired. By measuring the amplitudes of the fundamental frequency (first harmonic) and the second harmonic for different propagation distances, data pairs are gathered. According to equation (2.6), the nonlinearity parameter β is then determined by the slope of a linear fit to this data.

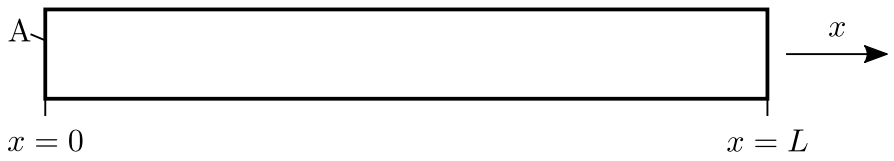

Figure 2.6: Thin bar specimen with length L and cross-section A. Adopted from [18].

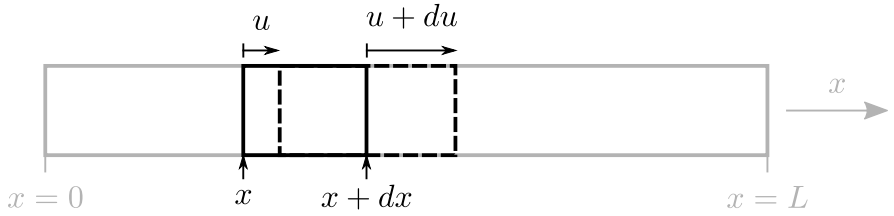

Figure 2.7: Arbitrary segment with length dx of the thin bar. Adopted from [18].

2.2 Wave Propagation in Materials

The following section describes the one-dimensional longitudinal behavior of thin bars and will introduce the stress, strain, longitudinal wave equation and the natural frequencies of a thin bar in free-free boundary conditions as shown by Kinsler [18].

2.2.1 Longitudinal Waves in a Thin Bar

Consider a thin bar with cross section A and length L whose main axis is oriented along the x-axis (Figure 2.6). All movement is to be considered uniform in any cross section. As shown in figure 2.7 an arbitrary segment of length dx is confined by a cross section at x and at $x + dx$. Assume a longitudinal force which causes a displacement of the cross sections by $u = u(x, t)$ to the right. Thus, the left-sided limitation of the segment is displaced by $u(x, t) = u$ and the right end moves a distance of $u(x+dx, t) = u+du$ in the positive x direction. For infinitesimal small dx the displacement $u(x+dx, t)$ can be represented by the first two terms of the Taylor's

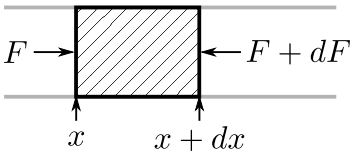

Figure 2.8: Free body diagram of the segment with length dx. Adopted from [18].

series expansion of u with respect to x:

$$u(x + dx, t) = u + du = u + \frac{\partial u}{\partial x}\, dx \tag{2.7}$$

Since the left and the right end of the segment move, the length after the deformation is given by

$$u(x + dx, t) - u(x, t) = u + du - u = du = \frac{\partial u}{\partial x}\, dx. \tag{2.8}$$

The strain is defined as the ratio between change in length and the original length. Thus,

$$\varepsilon = \frac{\frac{\partial u}{\partial x}\, dx}{dx} = \frac{\partial u}{\partial x} \tag{2.9}$$

defines the strain as a function of t and x. The displacements $u(x, t)$ of the cross sections of the bar are caused by the continuous force $F(x, t)$ which acts at every cross section. Consequently, on the left end of the segment a force $F = F(x, t)$ is acting. On the right end the force $F + dF = F(x + dx, t)$ is acting. Figure 2.8 shows the free body diagram of the segment of length dx. The right force can also be described by the first two terms of the Taylor's series expansion of $F(x, t)$ at x,

$$F + dF = F + \frac{\partial F}{\partial x} dx. \tag{2.10}$$

Assuming small strains it is possible to locally apply Hooke's Law, which gives a proportional relation between strain and stress:

$$\sigma = E \cdot \varepsilon \Leftrightarrow F = EA \cdot \varepsilon, \tag{2.11}$$

where E is the Young's Modulus, ε is the strain and the stress is defined as $\sigma = \frac{F}{A}$. Together with equation (2.9) and (2.10) this leads to

$$dF = AE \cdot \frac{\partial^2 u}{\partial x^2} dx. \tag{2.12}$$

The mass of the segment is

$$dm = A\rho \cdot dx. \tag{2.13}$$

where ρ is the mass density of the material. Because dx and thus du are considered infinitesimal small, the center of mass is assumed to move with the left limiting plane and thus the acceleration a of the segment is given by the second partial derivative in time of the displacement u:

$$a = \frac{\partial^2 u}{\partial t^2}. \tag{2.14}$$

Inserting (2.12), (2.13) and (2.14) into the equation of motion leads to

$$AE \cdot \frac{\partial^2 u}{\partial x^2} dx = A\rho \cdot dx \cdot \frac{\partial^2 u}{\partial t^2}$$

and is simplified to the one dimensional longitudinal wave equation,

$$\Leftrightarrow \frac{\partial^2 u}{\partial x^2} = \frac{1}{c^2} \cdot \frac{\partial^2 u}{\partial t^2} \tag{2.15}$$

where $c = \sqrt{\frac{E}{\rho}}$ is the phase velocity. The complex harmonic solution for the longitudinal wave equation is given by

$$\mathbf{u} = \mathbf{A}\, e^{i(\omega t - kx)} + \mathbf{B}\, e^{i(\omega t + kx)} \quad \text{with} \quad k = \frac{\omega}{c} \tag{2.16}$$

where $\mathbf{A}$ and $\mathbf{B}$ are the amplitudes of the right and left traveling waves and k is the wavenumber.

2.2.2 Longitudinal Eigenmodes of a Thin Bar in Free-Free Boundary Conditions

In free-free boundary conditions the two ends of the bar are assumed not to transmit any forces. This directly implies that the two ends have to be stress and strain free. For the example of a bar with length L the strain

$$\varepsilon = \frac{\partial u}{\partial x} \tag{2.17}$$

is equal to zero at $x = 0$ and $x = L$. The first boundary condition leads to

$$\mathbf{A} - \mathbf{B} = 0 \Leftrightarrow \mathbf{A} = \mathbf{B}. \tag{2.18}$$

Thus, right and left traveling waves always have the same amplitude and (2.16) reduces to

$$\mathbf{u} = \mathbf{A}\, e^{i\omega t} \cdot (e^{ikx} + e^{-ikx}) = 2\mathbf{A}\, e^{i\omega t} \cdot cos(kx) \tag{2.19}$$

The boundary condition at $x = L$ gives

$$-2\mathbf{A}k\, e^{i\omega t} \cdot sin(kL) = 0. \tag{2.20}$$

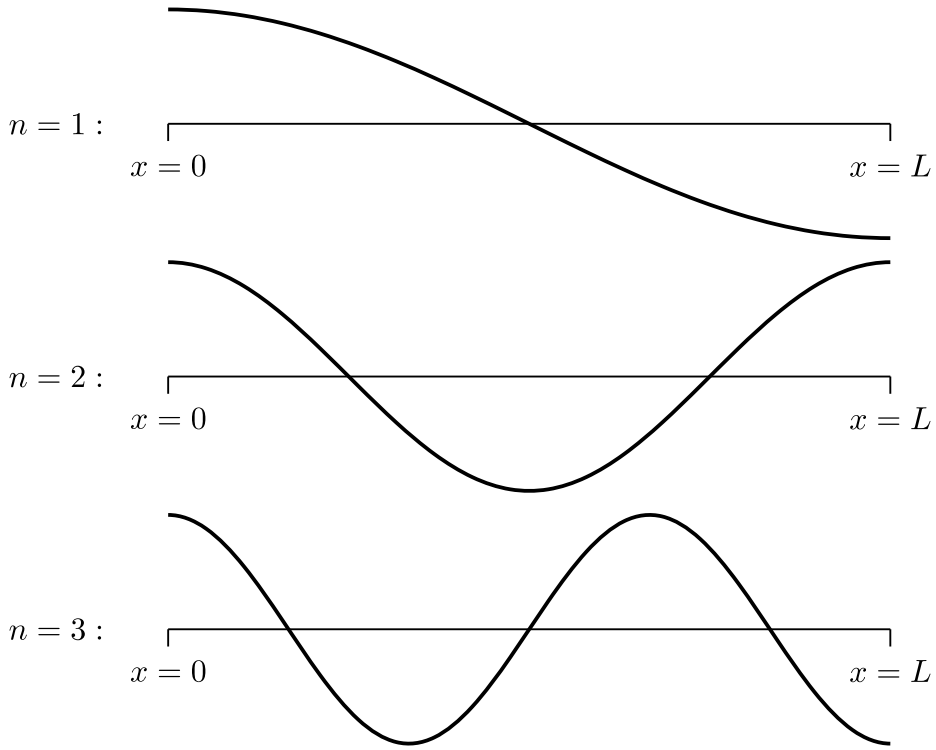

Figure 2.9: Three exemplary longitudinal modes of a thin bar in free-free boundary conditions. The three graphs display the displacement u of the first three natural frequencies. Adopted from [18].

There exists an infinite amount of solutions for this equation, called natural frequencies:

$$k_n = \frac{n\pi}{L} \quad \text{or} \quad f_n = \frac{nc}{2L} \quad \text{with} \quad n = 1, 2, 3, \ldots \tag{2.21}$$

These natural frequencies correspond to eigenmodes which are described by

$$\mathbf{u_n} = 2\mathbf{A}_n \, e^{i\omega_n t} \cdot cos(k_n x) \quad \text{with} \quad k_n = \frac{2\pi f_n}{c}, \;\; \omega_n = 2\pi f_n \tag{2.22}$$

and the first three eigenmodes are visualized in figure (2.9). This modes are so-called standing waves. This means the oscillation is solely described by a space dependent sinosoid. In (2.22) this part is represented by $cos(k_n x)$. Time dependent is nothing but the amplitude ($2\mathbf{A}_n \, e^{i\omega_n t}$). As expected in free-free boundary conditions the maximum displacements of all eigenmodes are always present at the boundary on

both ends.

CHAPTER 3
MATERIAL

3.1 Material

In the past, 9-12%Cr ferritic martensitic steels have attracted attention due to their high temperature performance. While these steels comply with the requirements for ultimate strength, creep strength and corrosion resistance, they are relatively cheap. Alternatives have poor thermal cycling capabilities (austenitic steels) or are around ten times more expensive (nickel based superalloys). In the 1950's the 12CrMoV steel X20 was developed. It marked a significant increase in creep strength compared to materials existing at this time. The modified Cr9Mo1 steel P91 (1970's) further improved and P92 (1980's) even doubled the creep strength of X20. Improved creep resistance is achieved by adding relatively small amounts of elements like vanadium (V), niobium (Nb), nitrogen (N), tungsten (W) and boron (B). [19]

In this work the modified ferritic martensitic steel Cr9Mo1 is examined. This steel has attractive properties for the power plant industry where high temperatures and high pressure are present. It is valued for its sufficient ultimate strength, low thermal expansion, resistance against corrosion and oxidation, adequate fatique resistance and high creep strength at service temperatures up to $650°C$. Furthermore, 9%Cr steel is relatively cheap compared to other materials which meet the same requirements. [20]

3.1.1 Chemical Composition and Mechanical Properties

The main alloy elements of modified Cr9Mo1 steel are chromium (Cr) and molybdenum (Mo). The full chemical composition is showed in table 3.1. Chromium is the main alloying element and ensures satisfying hot corrosion and high temperature

Table 3.1: Chemical Composition of modified Cr9Mo1.

Element	C	Mn	P	S	Si	Cu	Ni	Cr
Percentage [%]	0.117	0.443	0.02	0.0005	0.33	0.09	0.153	8.888
Element	Mo	Al	Nb	V	Ti	N		
Percentage [%]	0.862	0.011	0.073	0.192	0.003	0.0451		

Table 3.2: Mechanical properties of modified Cr9Mo1.

Yield strength $R_{0.2\%}$	620	MPa
Tensile strength R_m	755	MPa
Elongation A_{50}	26	%
Vickers hardness	235	HV10

oxidation resistance. Molybdenum is a the second important alloy and is needed for solution strengthening and improves the creep strength. The mechanical properties are summarized in table 3.2.

3.1.2 Heat treatment of Cr9Mo1

The material as it is received is normalized and tempered. The normalizing is done at $1050°C$. At this temperature, after a holding time of typically one to two hours, a fully austenitic microstructure is obtained. After cooling in air at room temperatures the steel becomes fully martensitic with a high dislocation density. The steel is hard and brittle at this point. To recover ductility the steel is tempered at $770°C$.

3.1.3 Thermal Aging

Thermal aging induces forming of precipitations in certain alloy steels and causes an increase of the hardness. The initially supersaturated element segregates by diffusion and forms finely distributed precipitations. These impurities hinder the free sliding

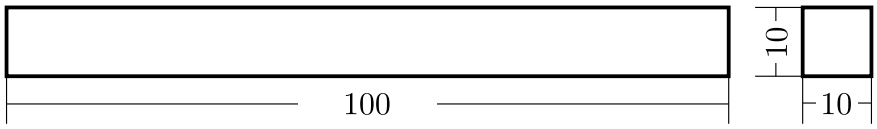

Figure 3.1: Geometry of the NRUS samples. All units are in mm.

Table 3.3: Heat treatment of samples.

Sample Designation	Temperature $[°C]$	Time $[h]$
Sample A	650	0
Sample B	650	200
Sample C	650	500
Sample D	650	1000
Sample E	650	1500
Sample F	650	3000

motion of dislocations and deformation requires higher external forces. Thus, this hardening effect is based on the increased number of precipitats which prevent dislocations to move freely and ultimately leads to a higher yield stress. This precipitation process can be divided into three stages: nucleation, growing and coarsening. Nucleation describes the aggregation to precipitates at for instance latter defects, growing is indicated by an increase in radius of the precipitates and coarsening describes the process when large precipitates start growing on the expense of smaller ones.

3.1.4 Specimen Preparation

Figure 3.1 shows the geometry of the specimens prepared for the NRUS measurement. They have a length of 100 mm and a cross section of 10 mm times 10 mm. Sufficient length to width ratio ensures that the pure longitudinal modes are excited. The heat treatments the samples undergo are listed in table 3.3. There are six specimens which are isothermally heat treated for 0 h, 200 h, 500 h, 1000 h, 1500 h and 3000 h respec-

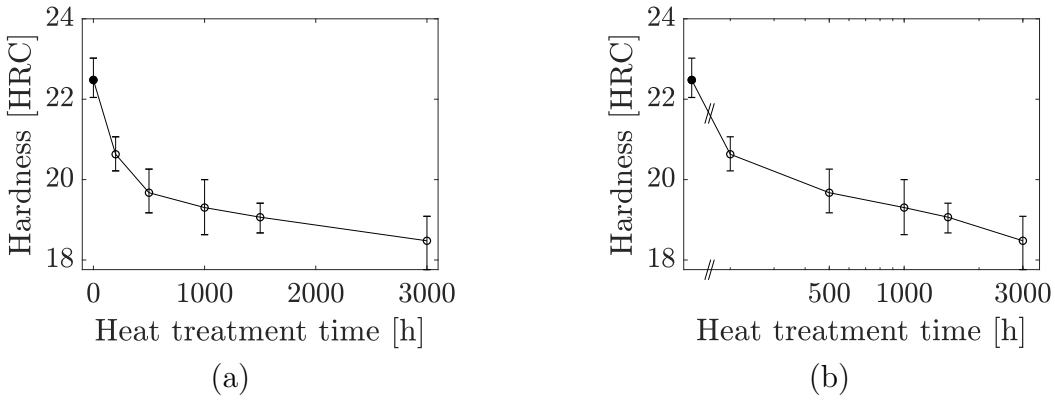

Figure 3.2: Rockwell C Hardness against heat treatment holding time at 650°C. The plots (a) and (b) show the same data, but (b) is plotted with a logarithmic x-axis. The filled dots indicate the hardness measurement after tempering without additional thermal aging. The x-axis in (b) is broken, because it is not possible to display 0 at a logarithmic scale.

tively. In the beginning the steps between exposure times are small to investigate the early stages of thermal aging more closely. The heat treatment was done for pieces with size approximately 200 mm ×45 mm ×13 mm. The NRUS specimens are then EDM-cut and the two end faces are sanded up to 2000 grid.

3.1.5 Material Condition

The following tests have already been performed by Marino et al. [21]. The measurements of hardness and classical quadratic nonlinearity (β) were performed on bigger specimens from which the smaller specimens for the NRUS measurements of this research were cut out. Thus, assuming the EDM-cutting of the thin bars did not change the microstructure, all measurements are done on specimens in identical conditions.

Rockwell C Hardness Measurements

Figure 3.2 shows a clear decrease of hardness for rising heat treatment time. Marino et al. [21] describe the behavior as a drastic decrease up to a holding time of 500 h and a gradually decreasing hardness for longer heat treatments (see (a)). The same

data plotted in (b) with logarithmic x-axis shows linearity. Thus, the behavior could be described as a logarithmic decline after a strong drop in the early stages of thermal aging.

Similar results are reported by Pešička et al. [22] and Wendell et al. [23]. Both studies also investigated modified Cr9Mo1 but their data show the evolution of hardness beginning from the martensitic state (after austenitizing and air cooling). The hardness measurements performed by Marino et al. show the hardness-heat treatment time dependence after an initial tempering at $770°C$. However, the relative decrease in hardness per decade, which the two studies report, almost coincide. Thus, the logarithmic dependence of the measured hardness is valid for a long range of heat treatment times. The decrease of hardness suggests that the dislocation density also decreases logarithmically over heat treatment time.

Classical Quadratic Nonlinear Parameter β

On the identical material used in this research, the classical quadratic nonlinearity parameter β was measured for all six heat treatment states. The measurements were done on bigger samples (200 mm $\times$ 45 mm $\times$ 13 mm) because of functional restrictions of this nonlinear Rayleigh wave technique due to a minimum wave propagation distance and an adequate contact surface for the exciting transducer wedge. Figure 3.3 shows the experimental results acquired by Marino et al. [21] for the relative quadratic nonlinearity parameter β' divided by the mean value of the normalized and tempered state (0 h heat treatment). The error bars indicate the highest and lowest value measured for each specimen. The last specimen has the largest error bars with a width of about 10 %. Despite that, the general trend is clearly recognizable. The figure shows an initial rapid decrease of β', followed by a increase after 500 h which even exceeds the initial value of β'. The drop in the beginning of about 30 % is explained by Marino et al. with the reduction of the dislocation density in this phase.

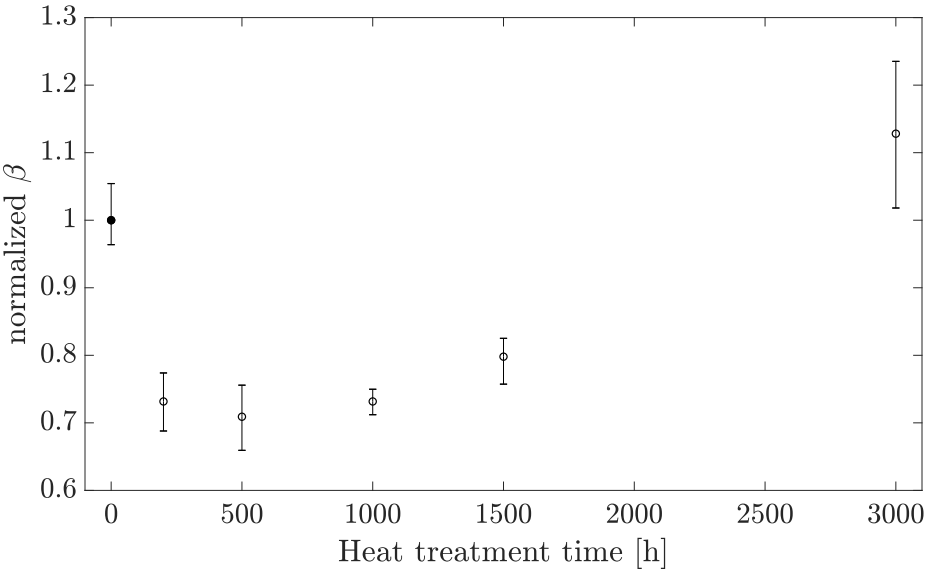

Figure 3.3: Normalized β against heat treatment time. The circles represent the mean value of all measurements for one specimen while the error bars indicate the highest and lowest value measured. The results are taken from Marino et al. [21].

The increase to 113 % of the initial value is reasonable because of precipitation nucleation and growth. Marino et al. conclude that the acoustic nonlinearity parameter is very sensitive to the microstructural evolution including changes in dislocations and precipitations.

CHAPTER 4
EXPERIMENTAL SETUP

4.1 Non-Contact Nonlinear Resonance Ultrasound Spectroscopy for Thin Bars

In this section, the experimental setup, first developed in [1] by Steffen Maier and then improved in this research, is introduced. This setup uses a non-contact air-coupled excitation. Thereby, unwanted influences of contact points are avoided. Because this NRUS measurement is based on the longitudinal resonance, it is especially important to avoid contact in the extension of the propagating direction. By avoiding contact, there is a high impedance mismatch at the two ends of the specimen and the interfaces lead to strong reflections.

4.1.1 Experimental Setup

A schematic of the experimental setup is shown in figure 4.1. A picture of the setup, as it is realized, can be found in figure 4.2. To realize best possible free-free boundary conditions, the thin bar specimen is positioned horizontally with two wire loops. For very small amplitudes and especially for longitudinal movements, this setup ensures sufficiently little constraints to the specimens movement. The laser vibrometer detects the out-of-plane velocity at one end of the sample. Thus, only longitudinal movement is detected. The sample's other end is excited by the air-coupled transducer which is extended with a focusing horn to maximize the energy transfer to the resonator. The laser vibrometer and the combination of transducer and focusing horn are attached to linear stages to be able to adjust the distances to the specimen as well as to ensure that the specimen is excited symmetrically and the movement is read at the

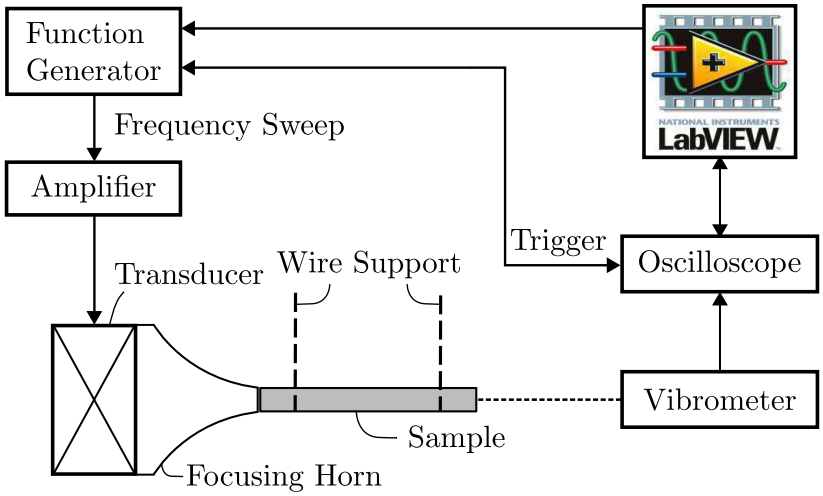

Figure 4.1: Schematic of the NRUS experimental setup. Adopted from [9].

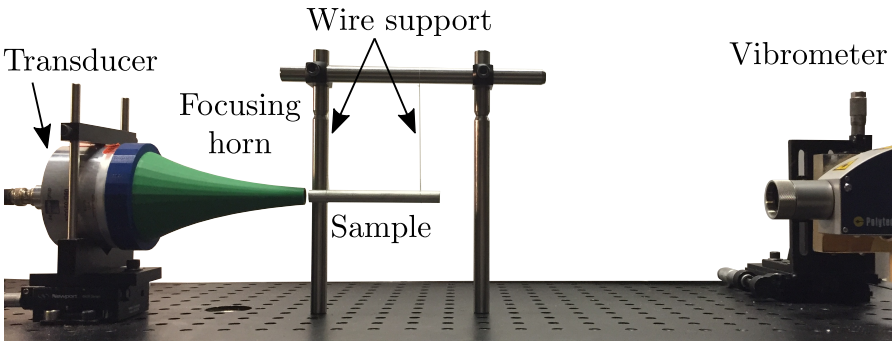

Figure 4.2: Picture of the NRUS experimental setup. Adopted from [9].

center of the end-plane. The transducer is driven by a E&I power amplifier which increases the amplitude output of the function generator by 55 dB. The oscilloscope reads the output of the laser vibrometer. The function generator is connected to the oscilloscope and triggers at the beginning of the linear sweep. This way the generation of resonance curves and the recording of the response are synchronized. The measurement is fully automated by a LabView routine which controls the function generator and the oscilloscope. The time domain signal is saved as a human readable csv-file which can be used in a Matlab script to post-process the gathered data.

4.1.2 Components

Transducer

To excite the sample, a NCG50-D50 circular non-contact transducer by The Ultran Group is used. This piezoelectric transducer has a diameter of 50 mm and a nominal frequency of 50 kHz and is used with a peak-to-peak driving amplitude up to 104 V, which is well under the limitations for continuous load.

Power Amplifier

A E&I 1040L power amplifier drives the transducer. The nominal amplification is 55 dB so that the peak-to-peak voltage of the function generator is multiplied by about 560. The amplifier is capable of outputting 400 Watts, covers frequencies between 10 kHz and 5 MHz and achieves a gain flatness of ± 1 dB. [24]

Function Generator

For generating sinusoidal frequency sweeps, an Agilent 33250A function generator is used. While keeping a constant amplitude, the frequency is linearly increased between set boundary frequencies. The function generator is capable of generating a signal with peak-to-peak voltage of 20 V.

Laser Vibrometer

A Polytech 1-dimensional laser doppler vibrometer is used in this research to measure the out of plane velocity at the end-face of the specimen. It is capable of measuring the velocity in a high frequency range. Build in low- and high-pass filter are set to 100 kHz and 100 Hz, respectively. In advantage to other techniques to monitor the movement, a laser vibrometer does not interfere with the measured system. Other types of sensors which need to be attached to the sample possibly change the results

by adding mass.

Oscilloscope

A Tektronix DPO5034B oscilloscope is used to measure the output of the laser vibrometer.

4.1.3 Measurement Procedure

The measurement principle for NRUS is a resonance frequency shift for increasing strain amplitude. When exciting the specimen with a frequency it will start vibrating with the same frequency. If the excitation frequency is close to a specific natural frequency, the amplitude will be significantly higher. In this case the excitation frequency is close to a resonance frequency of the specimen. To measure the resonance frequency as well as the resonance amplitude, the specimen is excited with a linear frequency sweep. This sweep is centered around the expected resonance frequency, which causes the response received by the laser vibrometer to have a maximum approximately at the center of the signal. This maximum represents a value pair of resonance frequency and resonance amplitude. The resonance curves are done for equidistant excitation amplitude steps. To be able to compensate for temperature variation and other environmental influences, every second measurement is a resonance measurement done at a reference excitation amplitude. Figure 4.3 visualizes the sequence of excitation amplitudes for a measurement. The measurements represented by the red dots are done for progressively increasing excitation amplitude and are called measurement for varying excitation amplitudes (MVA). The black dots symbolize the measurements at reference excitation amplitude (MRA).

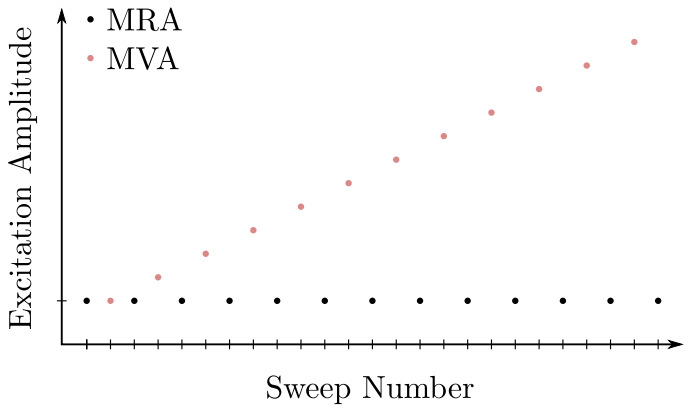

Figure 4.3: Excitation Amplitude Sequence of 25 measurements. The $N = 12$ red dots indicate measurements with increasing excitation amplitudes whereas the black dots are measurements at constant excitation amplitude.

4.1.4 Post-processing

The large amount of data gathered during the measurement is analyzed in Matlab. All time domain signals are analyzed in order to find the resonance frequency as well as the resonance amplitude. In the following, the procedure is explained with an exemplary signal. Figure 4.4 shows the time domain signal with an applied window function, which reduces the leakage effect caused by the finite duration of the signal. The plot in figure 4.5 represents the frequency domain response, generated by a Fast Fourier Transform (FFT). The maximum value of the Fourier transform is determined and a third order polynomial approximates a small range around the peak. The maximum of the polynomial represents a value pair of resonance frequency and corresponding resonance amplitude. This procedure is repeated for all the signals generated at increasing excitation amplitudes (see Figure 4.3) and the results for the varying amplitudes are visualized in figure 4.6. The resonance frequencies clearly show a shift to lower values for increasing excitation amplitudes. The nonclassical hysteretic nonlinearity parameter α is defined in (2.3) by

$$\frac{\Delta f}{f_0} = \alpha \hat{\varepsilon}$$

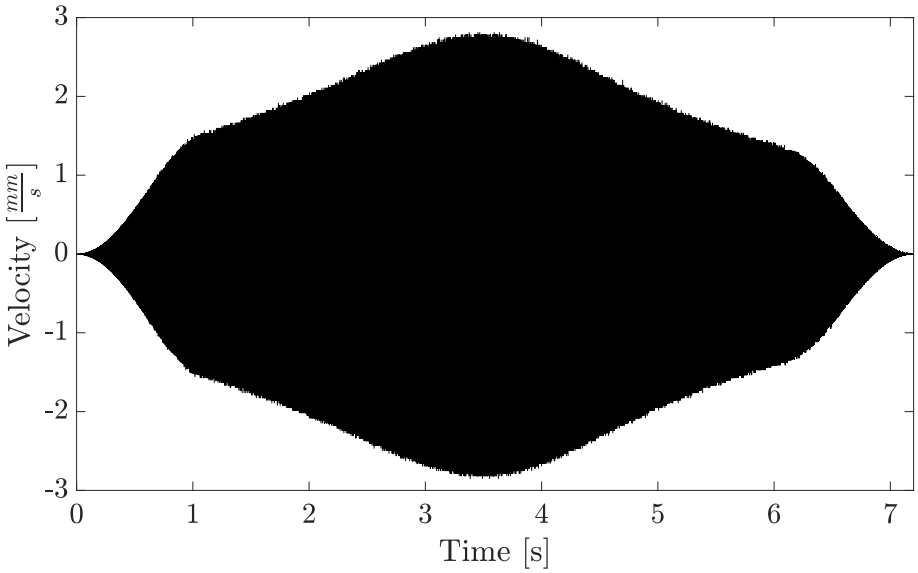

Figure 4.4: Time domain signal with an applied window function.

with the resonance frequency at an infinitesimal small amplitude f_0, the change of resonance frequency $\Delta f = f - f_0$ and the strain amplitude $\hat{\varepsilon}$. The resonance frequency at vanishing excitation amplitude is determined by fitting a line to the found maximum values of the resonance curves. The linear fit is then evaluated at zero amplitude to acquire f_0. Because the laser vibrometer measures the end-plane velocity, which is not directly related to the maximum strain in the specimen, an analytic relationship between velocity and strain is necessary. This relationship relies on the geometry and the assumption of pure harmonic waves. As described in chapter 2, the displacement throughout the thin bar specimen in case of resonance is expressed as

$$\mathbf{u}_n = 2\mathbf{A}_n \, e^{i\omega_n t} \cdot cos(k_n x) \quad \text{with} \quad n = 1, 2, \ldots . \tag{4.1}$$

The strain is defined in (2.17) as

$$\boldsymbol{\varepsilon} = \frac{\partial \mathbf{u}}{\partial x}$$

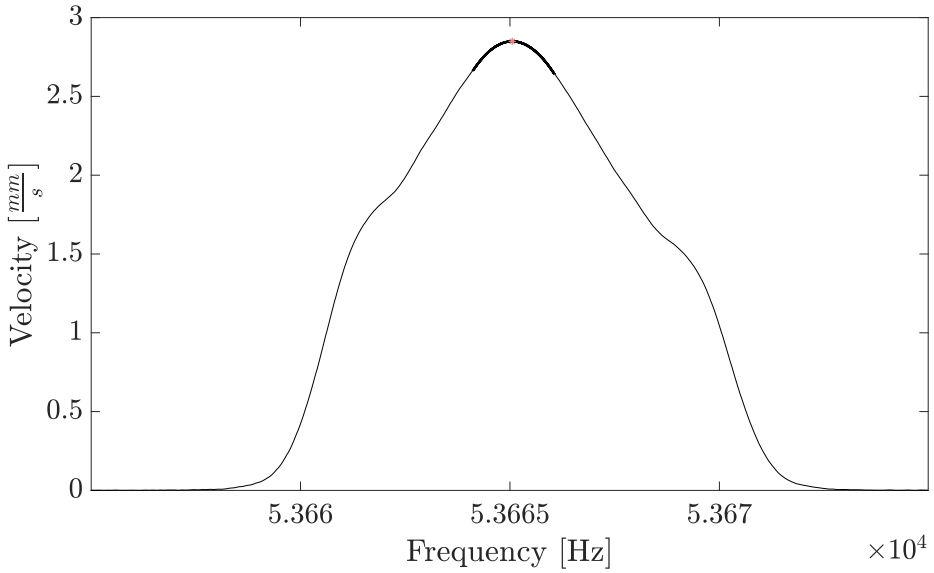

Figure 4.5: Frequency domain response, generated by a Fast Fourier Transform (FFT). The thick black line is a third order polynomial which approximates a small range around the peak of the FFT and is used to determine the resonance frequency and amplitude.

and thus, together with equation (4.1), the strain in case of resonance is

$$\boldsymbol{\varepsilon}_n = k_n \cdot 2\mathbf{A}_n \, e^{i\omega_n t} \cdot sin(k_n x). \tag{4.2}$$

The strain, like the displacement, is a standing wave in resonance conditions and the maximum strain is present at the position defined by $sin(k_n x) = 1$ for all times t:

$$\hat{\boldsymbol{\varepsilon}}_n = k_n \cdot 2\mathbf{A}_n \, e^{i\omega_n t} \tag{4.3}$$

The velocity v is defined as

$$\mathbf{v} = \frac{\partial \mathbf{u}}{\partial t} \tag{4.4}$$

and can be expressed in terms of resonance conditions as follows:

$$\mathbf{v}_n = i\omega_n \cdot 2\mathbf{A}_n \, e^{i\omega_n t} \cdot cos(k_n x). \tag{4.5}$$

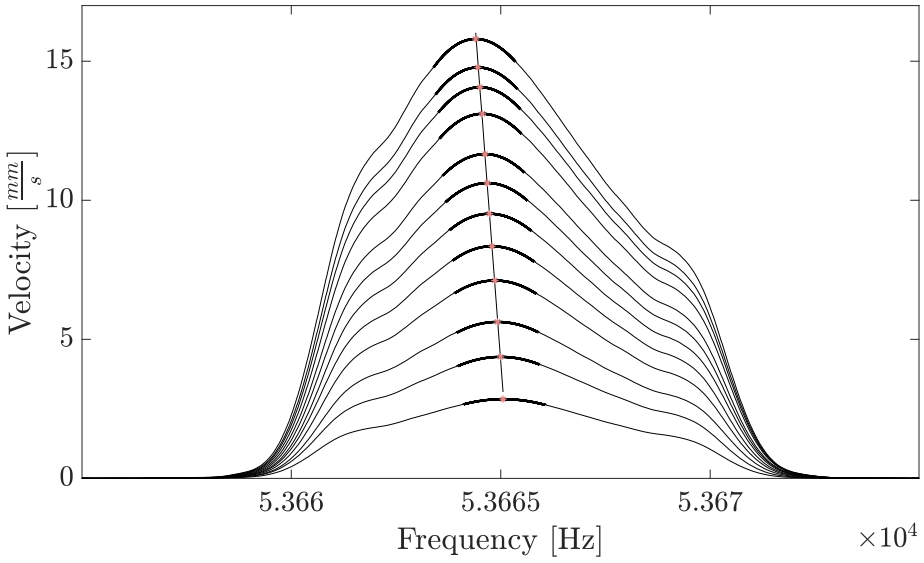

Figure 4.6: Frequency domain responses, generated at increasing excitation amplitude steps. The linear fit of the maximum values of each resonance curve is evaluated at zero amplitude to determine f_0.

As expected, the velocity is 90° phase shifted in time to the displacement as well as the strain. The desired strain amplitude $\hat{\varepsilon}$ is the magnitude of the complex valued maximum strain $\hat{\boldsymbol{\varepsilon}}_n$

$$\hat{\varepsilon} = |\hat{\boldsymbol{\varepsilon}}_n| = k_n \cdot 2|\mathbf{A}_n| \tag{4.6}$$

and the maximum velocity, present at $cos(k_n x) = 1$, is

$$\hat{v} = \omega_n \cdot 2|\mathbf{A}_n|. \tag{4.7}$$

With

$$k_n = \frac{\omega_n}{c}$$

equation (4.6) and (4.7) combine to

$$\hat{\varepsilon} = \frac{\omega_n}{c} \cdot 2|\mathbf{A}_n| = \frac{\hat{v}}{c} \tag{4.8}$$

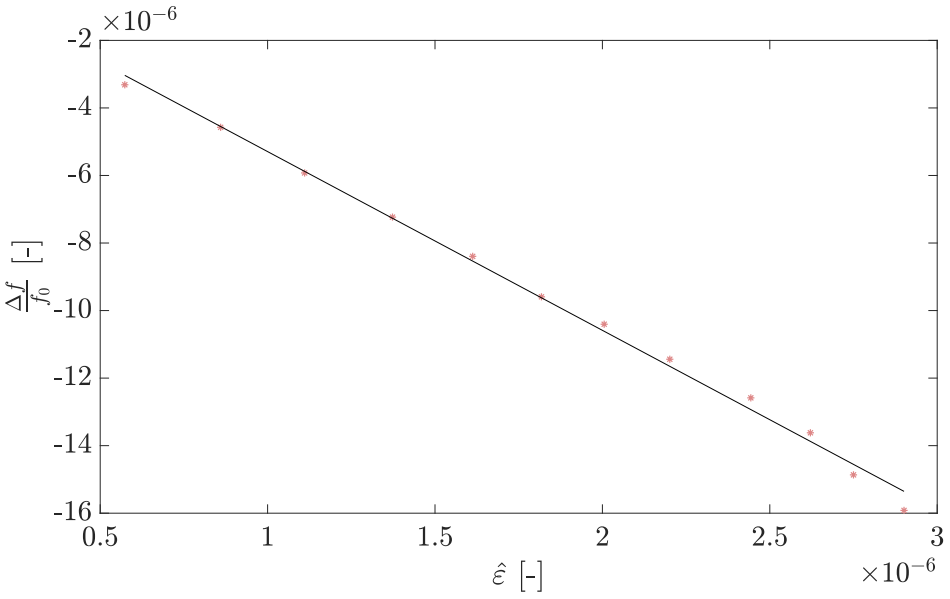

Figure 4.7: Plot of the maximum strain $\hat{\varepsilon}_i$ against the relative resonance frequency shift $\frac{\Delta f_i}{f_0}$ with $\Delta f_i = f_i - f_0$ for $i = 1 \dots N$. The black solid line represents the best linear fit in a least square sense (4.12).

The longitudinal wave velocity c is defined by (2.21) as

$$c = \frac{2 f_n L}{n}. \tag{4.9}$$

Thus, the maximum strain in the specimen is

$$\hat{\varepsilon} = \frac{\hat{v} n}{2 L f_n} \tag{4.10}$$

and can consequently be determined by measuring the maximum velocity at the end-planes. Together with equation (2.3) the relation between the measured physical quantities, frequency and out of plane velocity, can be established:

$$\frac{\Delta f}{f_0} = \alpha \frac{\hat{v} n}{2 L f_n}. \tag{4.11}$$

Figure 4.7 plots the maximum strain of the ith measurement $\hat{\varepsilon}_i$ against the relative

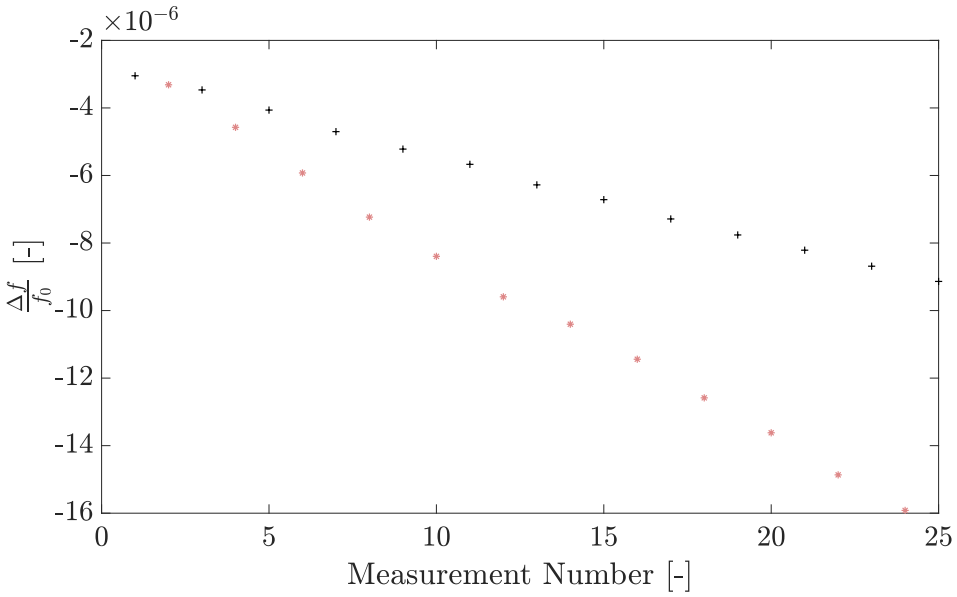

Figure 4.8: Frequency shift for varying excitation amplitude in comparison to the reference measurements.

resonance frequency shift $\frac{\Delta f_i}{f_0}$ with $\Delta f_i = f_0 - f_i$ for $i = 1 \dots N$. The black solid line represents the best linear fit in a least square sense. Thus the linear fit approximates α so that the cost

$$Q = \sum_{i=1}^{N} \left(\frac{\Delta f_i}{f_0} - \alpha \hat{\varepsilon}_i \right)^2 \tag{4.12}$$

is minimal. The y-intercept of the linear fit has to be zero within numerical accuracy because of the definition of Δf_i. With this procedure the nonclassical hysteretic nonlinearity parameter α is found to be -5.29. The root mean squared error (RMSE) of the linear fit is defined by

$$\text{RMSE} = \sqrt{\frac{Q}{N}} \tag{4.13}$$

and calculates to RMSE $= 2.57 \cdot 10^{-7}$. Under perfect ambient conditions, the reference measurements acquired in between the data points visualized in figure 4.7 should lead to constant results. Figure 4.8, which shows the results for the reference measurements together with the results for varying excitation amplitudes, reveals a change in resonance frequency for constant excitation. This is due to ambient temper-

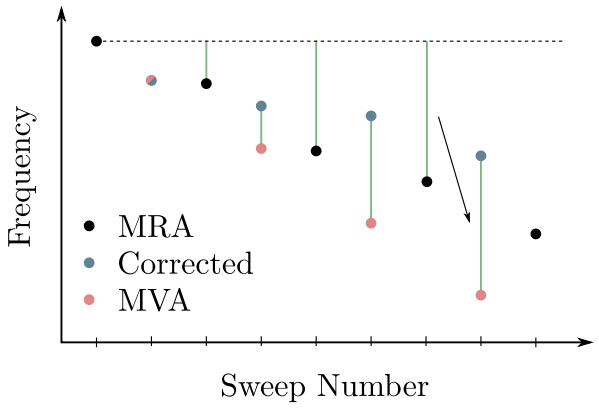

Figure 4.9: Schematic of the correction procedure adopted from Haupert et al. [6]. The corresponding green lines have the same length. The figure is based on fictional data.

ature changes and shows that the results for α without correction are not meaningful. Therefore, a methodology adopted from Haupert et al. [6] that compensates temperature changes during the measurements, is included. This procedure takes the first MRA as a baseline. Every MVA is then corrected by the difference of the according reference measurement to the first reference measurement. The methodology is visualized in figure 4.9. The measurements are equidistant in time and the approximate time domain distance is 40 seconds. To minimize temperature deviations, the measurement setup is enclosed in a simple cardboard cover. Nevertheless, the correction largely changes the result of the measurement. The linear fit using the corrected resonance value pairs leads to an α value of -2.85. The RMSE decreased by 30 % to $1.79 \cdot 10^{-7}$.

4.1.5 Measurement Improvements

Positioning

Originally, the specimen hung on two fixed length wires. The positioning relied on friction and achieving precision was effortful. With the new fixture, the specimen hangs in two loops whose two ends can be elongated or shortened. This way, within

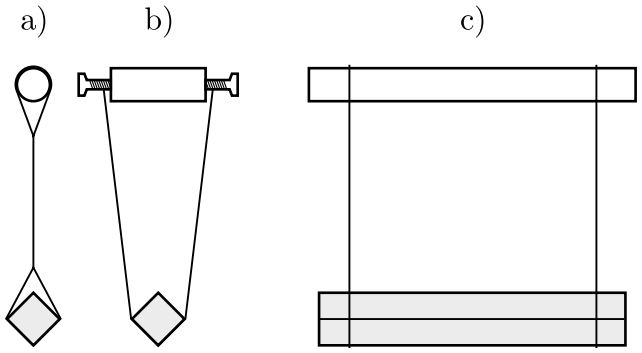

Figure 4.10: Schematic comparison of the old against the improved positioning. The previous setup is displayed in (a) while the new fixture with screws to position both ends of the specimen separately is shown in (b). (c) shows the side view of both positionings.

its limits, a precise positioning in all six directions is possible. Figure 4.10 visualizes both fixtures. The old fixture is displayed in longitudinal direction in (a). With the new setup, displayed in (b), the position can be adjusted by turning the screws in or out. The two screws furl the wire so that it can be elongated or shortened. Because the specimen hangs in two wire loops, the second loop prevents it from rotating around its long axis. The side view is displayed in (c). The new fixture adds constraints in the transversal direction. However, the longitudinal direction, important for this measurement, stays unaffected.

Measurement Procedure

The measurement procedure stays almost unchanged. However, the excitation amplitude sequence is varied. Instead of executing 12 MVAs with 13 MRAs, the α measurement is expanded to 48 MVAs and 48 MRAs. This way the measurement can run longer without disturbance. Furthermore, the excitation amplitude sequence is changed so that when executing the MVAs the excitation amplitude is not exclusively raised. During one α measurement, the excitation amplitude is raised up to the maximal value, decreased to the lowest value and then increased and decreased again.

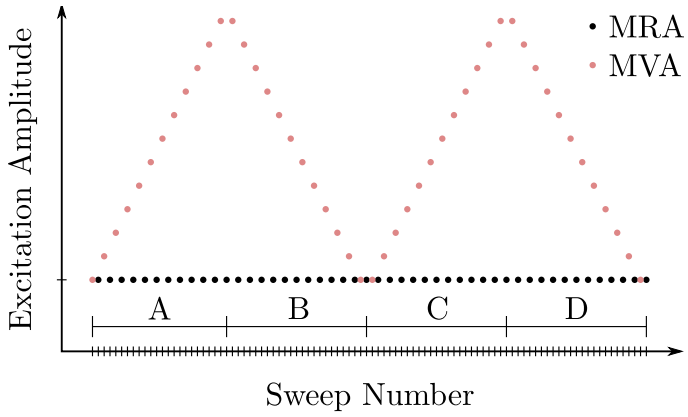

Figure 4.11: New excitation amplitude sequence. The excitation amplitude is not exclusively raised during the measurement. It goes up and down between the maximum and minimum amplitude.

The new sequence is displayed in figure 4.11. The advantage of this modification is that possible ambient effects, material effects like slow dynamics or discrete memory and changes in the measurement equipment, like warming of the transducer act with opposite sign on the measurement.

For example, suppose a linear increase of the environmental temperature. This increase will effect the measurement towards lower resonance frequencies and in section A in figure 4.11 it leads to an increased shift of frequency and thus an overestimation of α. In Section B, the still increasing temperature leads to a weakening of the shift induced by the rising amplitude, so an underestimation of alpha. When all the data is evaluated with a linear fit to obtain α this effect naturally cancels out.

Post Processing

The correction procedure adopted from Haupert et al. [6] uses the previous MRA to correct for environmental effects. Because there is an approximate distance of 40 seconds between every measurement, this procedure does not account for the change of the influencing effects in this time. When the influences change linearly over time, this error is mostly constant and will not effect the quality and result of the α

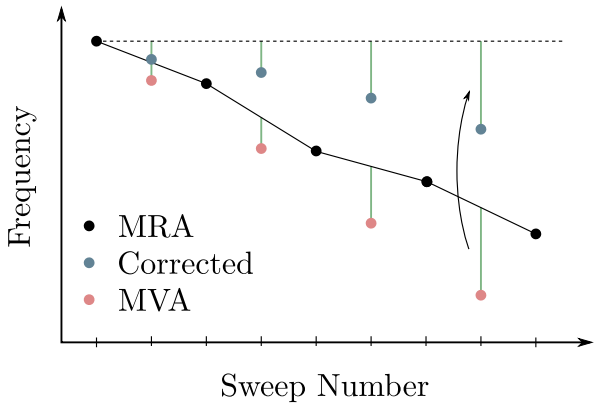

Figure 4.12: Schematic of the improved correction procedure. The corresponding green lines have the same length. The figure is based on fictional data.

measurement. However, if there is a change of slope this error will as well change its value. This can have a significant effect on the quality of the measurement. Because the environmental effects can be assumed continuous, an easy method to improve the correction to be slope independent is to refer a MVA to its both neighbors. The influencing effect is assumed to change linear between the two MRA and as a first approximation the mean resonance frequency of those two MRAs is used for the correction of the MVA. A visualization of this improved correction is shown in figure 4.12. To demonstrate the benefits of the improved correction procedure a measurement with a (possibly) nonlinear ambient influence is shown in figure 4.13. In (a) the resonance frequency of every measurement is plotted against the measurement number. The black crosses, representing the MRAs, change slightly nonlinear over the course of the measurement. In (b) and (c) the results of the simple correction is compared to the improved correction. The coefficient of determination decreases in this example from 0.992 to 0.991. This new procedure is more robust against ambient factors, thus the reproducibility of the measurement is enhanced.

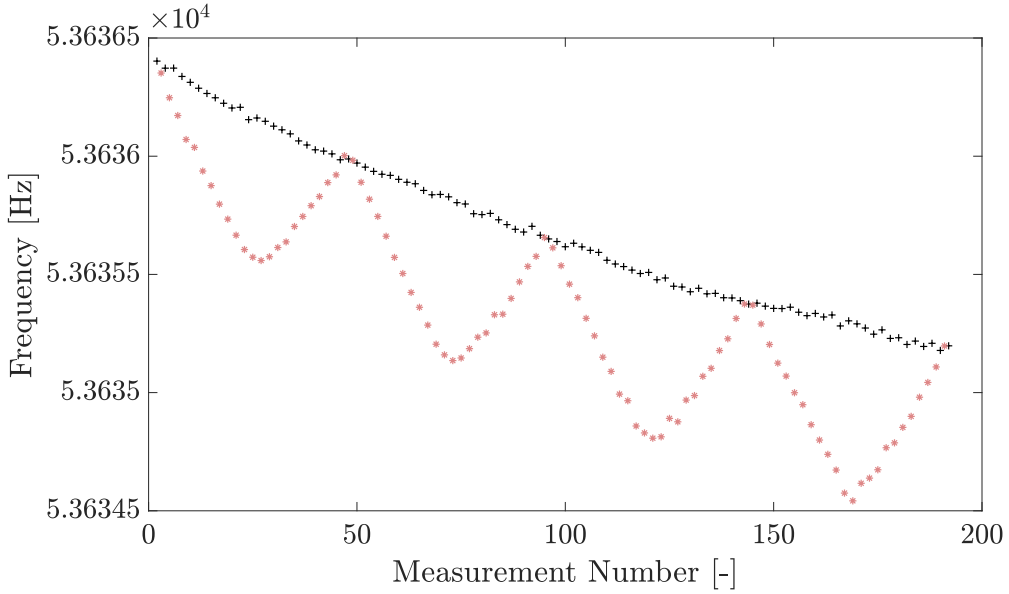

(a) Resonance frequency of MRAs (black crosses) and MVAs (red stars) against measurement number.

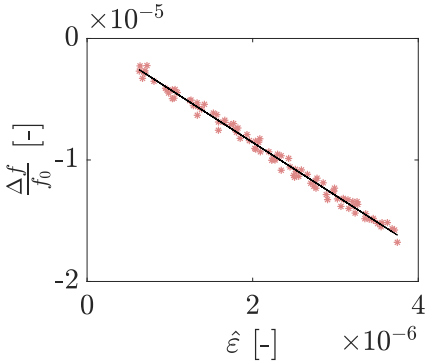

(b) Corrected relative frequency shift against strain amplitude. The values are corrected by the simple correction procedure. The coefficient of determination of the linear fit visualized in black is 0.992.

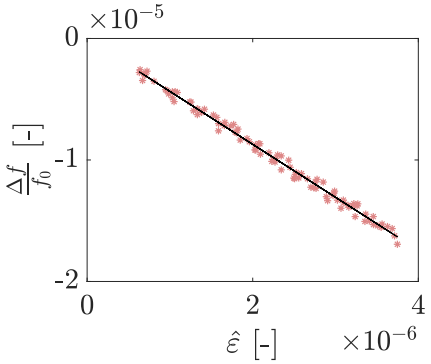

(c) Corrected relative frequency shift against strain amplitude. The values are corrected by the improved correction procedure. The coefficient of determination of the linear fit visualized in black is 0.991.

Figure 4.13: Comparison of the correction method by Haupert et al. [6] and the improved correction.

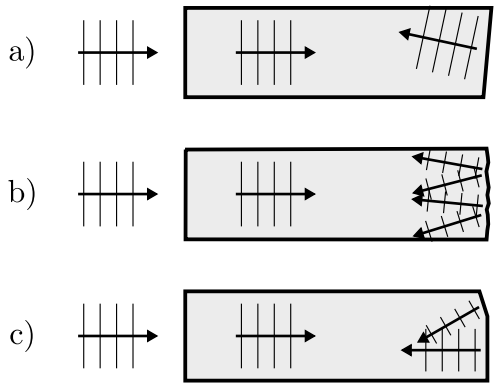

Figure 4.14: Schematic of misalignment (a), roughness (b) and poor flatness (c).

Specimen Preparation

Special attention was given to the specimen preparation. To achieve best possible resonance, the two end surfaces of the sample are carefully machined on the surface grinder. In this way, it is assured that the reflecting surfaces of the resonator are parallel and flat within high precision. The resonance in the specimen is based on left and right traveling waves which interfere with each other in a way that the waves form a standing wave (see chapter 2.2). Misalignment, roughness and poor flatness causes (parts of) the waves to interact with the other walls of the specimen and thus progressively deviate from the plane wave assumption. When a wave is reflected at, for example, a misaligned surface, the wave will reflect along a propagation direction not parallel to the main axis of the specimen. Additionally, every non-perpendicular reflection will cause shear waves. Shear waves usually have a lower wave speed and thus resonate at different frequencies and do not contribute to the desired resonance. Figure 4.14 schematically visualizes misalignment (a), roughness (b) or poor flatness (c).

CHAPTER 5
INFLUENCE OF AMBIENT TEMPERATURE

5.1 Temperature Measurement

The measurement setup is extended by a temperature measurement to better understand the different ambient effects influencing the measurement. To measure the temperature, a thermally-sensitive resistor (called thermistor) with negative temperature coefficient (NTC) is used. The nonlinear dependence between temperature T and resistance R_T is determined by the component characteristics β_{th} and R_{25} (resistance at $25°C$):

$$T(R_T) = \left[\frac{1}{273.15K + 25K} - \frac{ln\left(\frac{R_{25}}{R_T}\right)}{\beta_{th}} \right]^{-1}. \tag{5.1}$$

All temperature values in (5.1) are given in Kelvin. Figure 5.1 shows a picture of the used thermistor, which is out of the NTCALUG01A series by Vishay BCcomponents. A detailed description of the thermistor can be found in the datasheet [25]. The used NTC thermistor is characterized by $\beta_{th} = 4190$ K and $R_{25} = 100\,000\ \Omega$. The thermistor is integrated in a simple voltage divider circuit, which is visualized in figure 5.2. The circuit consists of a constant resistor ($100\,000\ \Omega$) in series with the thermistor. The voltage divider reduces the input voltage V_{in} to V_{out}. The output voltage is dependent on the resistance of the thermistor and the resistance of the thermistor can be determined by

$$R_T = \frac{V_{in}}{V_{out}} \cdot 100k\Omega - 100k\Omega. \tag{5.2}$$

A simple laboratory power supply is used to ensure a constant voltage $V_{in} = 17V$. The output voltage V_{out} is measured with the oscilloscope for the duration of the

Figure 5.1: Image of the used thermistor. It has a nominal resistance of $R_{25} = 100\,000\ \Omega$ at $25°C$. The nonlinear resistance-temperature curve is characterized by $\beta_{th} = 4190$ K. [25]

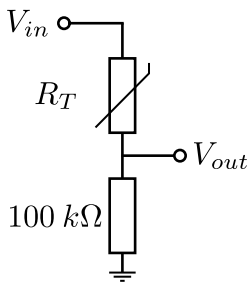

Figure 5.2: Circuit to measure the resistance of the thermistor. The voltage divider reduces the input voltage $V_{in} = 17$ V to V_{out}. The output voltage is dependent on the resistance of the thermistor and is measured with the oscilloscope.

sweep and LabView records these values and saves the average. From equation (5.1) and (5.2) follows

$$T(V_{out}) = \left[\frac{1}{273.15K + 25K} - \frac{ln\left(\frac{R_{25}}{\frac{V_{in}}{V_{out}} \cdot 100k\Omega - 100k\Omega}\right)}{\beta_{th}} \right]^{-1} \tag{5.3}$$

which gives the relationship between measured voltage V_{out} and the temperature at the resistor T. Thus, the temperature can be recorded for each resonance measurement (MVA and MRA). The temperature sensor is placed right next to the specimen to ensure that both specimen and sensor are similarly influenced.

5.2 Theoretical Influence of Temperature on the Resonance Frequency

At room temperatures and for small temperature changes the Young's modulus of the specimen can be assumed to change linearly with temperature. Most common steels behave linearly to temperature changes above about 100 K [26]. The behavior of Cr9Mo1, the steel considered in this work, does not fall out of line [27]. Thus, the Young's modulus' empirical dependence on the temperature T can be written as

$$E(T) = E_0 - aT \tag{5.4}$$

where E_0 is the Young's modulus at zero Kelvin and a acts as a proportionality factor. E_0 does not have a physical meaning because the temperature behavior of the Young's modulus is highly nonlinear for temperatures close to the absolute zero.

Equation (2.21) together with the phase velocity $c = \sqrt{\frac{E}{\rho}}$ gives the resonance frequencies in free-free boundary conditions for longitudinal waves in a thin bar specimen:

$$f_n = \frac{n\sqrt{\frac{E}{\rho}}}{2L} \quad \text{with} \quad n = 1, 2, \ldots \tag{5.5}$$

When the Young's modulus changes with temperature this will also effect the resonance frequencies. From equation (5.5) directly follows that the resonance frequency is proportional to the square root of Young's modulus

$$f_n \propto \sqrt{E}. \tag{5.6}$$

Equations (5.4) and (5.6) lead to the proportionality

$$f_n^2 \propto T + b \tag{5.7}$$

where b is a shift originated in equation (5.4).

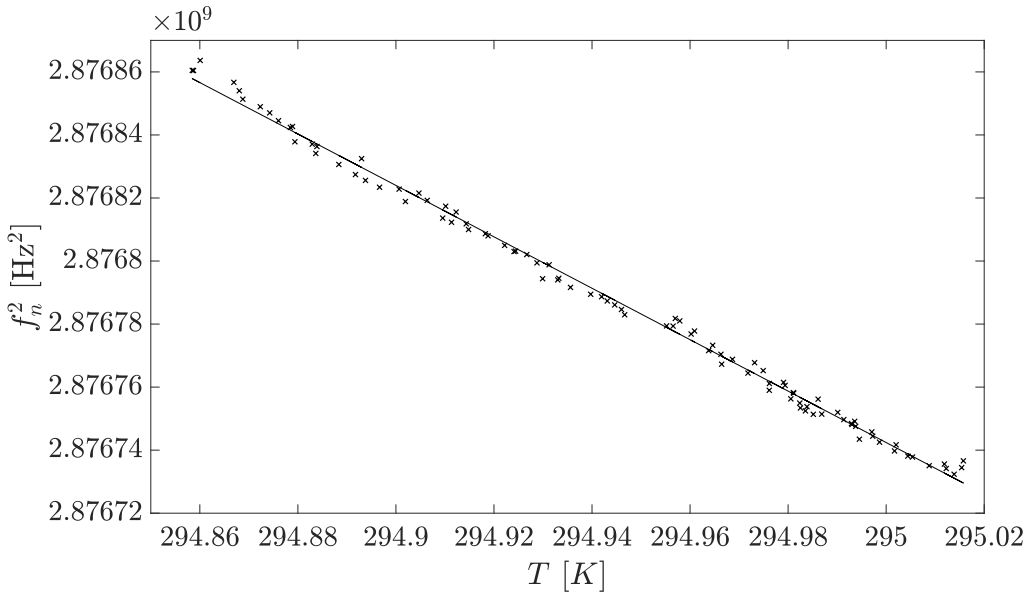

Figure 5.3: The square of the resonance frequency plotted against the temperature. The black line represents the best linear fit in least squares sense.

5.3 Validation of the Theoretical Influence of Temperature on the Resonance Frequency Based on Experimental Data

Figure 5.3 shows the square of the resonance frequency plotted against the temperature, recorded during the MRAs. The black line represents the best linear fit in least squares sense. The RMSE of the residuals between the data and the linear fit is RMSE = 2469.62 Hz^2. The coefficient of determination R^2 is 0.996 and thus indicates a strong linear correlation between temperature and the squared resonance frequency. This very good agreement of the data points with a linear fit strengthens the assumption that the deviation under constant measurement conditions is mainly due to ambient temperature changes. Other effects (e.g. slow dynamics) would lead to a deviation from this linear fit. Because of a value of R^2 near 1 for this regression on temperature, the influence of other environmental changes are by far of minor importance. Haupert et al. already suspected the dominating effect of ambient temperature in [6]. This research strongly confirms this assumption.

5.4 Young's Modulus Measurement Based on Temperature Measurement

Linear resonance ultrasound spectroscopy (RUS) is used to extract the elastic constant (Young's modulus) of a specimen with known geometry, density and therefore known resonance frequencies. The theoretical deviation in section 5.2 can be used to gain a temperature dependent formulation of the Young's modulus. Equation (5.7) states a proportionality between the square of the resonance frequency and the temperature shifted by b. The linear fit quantifies this dependence:

$$f_n^2 = AT + B \tag{5.8}$$

with the slope A and intercept B of the linear fit. Together with equation (5.5)

$$\frac{n^2 E}{4L^2 \rho} = AT + B \tag{5.9}$$

follows. When solved for the Young's modulus, one obtains

$$E(T) = (AT + B) \cdot \frac{4L^2 \rho}{n^2} \tag{5.10}$$

with the slope A and intercept B of the linear fit of f_n^2 over T. The specimen length L, mass density ρ and modenumber n are determined by the experiment and are also included in this equation. The data in figure 5.3 leads to the regression parameters $A = -8.16 \cdot 10^5 \, \frac{\mathrm{Hz}^2}{\mathrm{K}}$ and $B = 3.12 \cdot 10^9 \, \mathrm{Hz}^2$. Thus, the Young's modulus turns out as

$$E(T) = -6.17 \cdot 10^7 \, \frac{\mathrm{Pa}}{\mathrm{K}} \cdot T + 2.36 \cdot 10^{11} \, \mathrm{Pa}. \tag{5.11}$$

and can be evaluated at $T = 20°C = 273.15 \, \mathrm{K} + 20 \, \mathrm{K}$ by

$$E_{20} = E(293.15 \, \mathrm{K}) = 217.55 \, \mathrm{GPa}. \tag{5.12}$$

With this method, a temperature corrected measurement of the Young's modulus is possible and a precise climate chamber is not necessary. A major flaw of the presented procedure is that the influence of the amplitude is not put to account.

CHAPTER 6
RESULTS

6.1 NRUS

Non-contact nonlinear resonance ultrasound spectroscopy measurements are executed as described in chapter 4. For each specimen the excitation amplitude sequence visualized in figure 4.11 is run twice. Thus, one α measurement consists of 96 corrected data points for varying excitation amplitudes. Between the two sequences there is only a very short break to start the next sequence. The post processing is done for all measurements of one specimen at once and only one final nonlinearity parameter α is determined. Thus, the goodness of this measurement cannot be quantified by representing the multitude of measured α. Instead, the coefficient of determination R^2 of the linear fit to acquire α serves as a quality measure. Table 6.1 lists the α measurements for each specimen together with the corresponding R^2. Figure 6.1 displays the measured α values for the specimen with errorbars representing the standard error of α as estimated by the linear fit. The measurements show a strong drop of $|\alpha|$ in the beginning of the heat treatment. After 500 h holding time the absolute non-classical nonlinearity increases again and reaches a value close to the initial state (0 h heat treatment). The initial drop lowers the $|\alpha|$ value to about 55 %. Thus, α seems to be highly sensitive to microstructural changes.

6.2 Influence of Ambient Temperature

It has been shown in section 5.2 that there is a linear relation between the temperature T and the square of the n-th resonance frequency f_n^2. An exemplary dataset strongly confirms this correlation (section 5.3). Table 6.2 lists the coefficients of determination,

Table 6.1: Results of non-classical nonlinear parameter α measurements.

Sample Designation	Heat Treatment Time at 650°C [h]	α [-]	R^2 [-]
Sample A	0	-4.34	0.9956
Sample B	200	-2.67	0.9936
Sample C	500	-2.40	0.9874
Sample D	1000	-2.61	0.9363
Sample E	1500	-3.00	0.9961
Sample F	3000	-4.30	0.9920

Table 6.2: Coefficient of determination for the assumption of a linear relation between temperature and the square of the resonance frequency

Sample Designation	Heat Treatment Time at 650°C [h]	ΔT during measurement [K]	R^2 [-]
Sample A	0	0.08	0.9691
Sample B	200	0.23	0.9969
Sample C	500	0.51	0.9995
Sample D	1000	0.17	0.9936
Sample E	1500	0.43	0.9955
Sample F	3000	0.16	0.9957

which quantifies the goodness of the linear fit, together with the overall temperature change during the measurement for all six specimen. The minimal R^2 value of 0.9691 is observed at sample A, which also experienced the lowest change of temperature during the measurement. All in all, a linear relation between the temperature and the square of the resonance frequency could be confirmed for all the specimen.

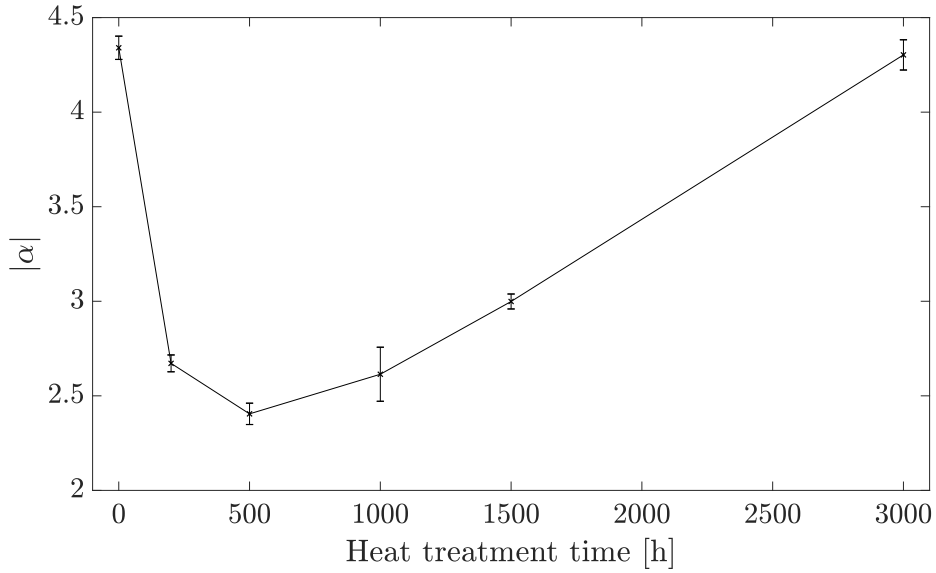

Figure 6.1: $|\alpha|$ of the Cr9Mo1 specimen plotted over heat treatment time. The errorbars indicate $\pm 2\sigma$.

6.3 Young's Modulus Measurement Based on Temperature Measurement

The procedure described in section 5.4 leads to a Young's modulus at $20°C$ for every specimen. The results are listed in table 6.3 and displayed in figure 6.2. The Young's modulus experiences a step from around 217 GPa to 218 GPa at the first heat treatment and then stays at about the same level. A slight decrease of the Young's modulus at higher heat treatment times is only supported by one measurement and thus will not be considered in this work. All in all, the changes in E are below 0.6 % compared to the initial value and are thus very weak. Taking into account that the effect of the amplitude is not considered, these small changes are not significant. However, these measurements show that the measurement of Young's modulus does not strongly react on microstructural changes and is not sufficient to monitor them.

Table 6.3: Results of Young's modulus measurements.

Sample Designation	Heat Treatment Time at 650°C [h]	Young' Modulus at 20°C [GPa]	R^2 [-]
Sample A	0	216.97	0.9691
Sample B	200	217.93	0.9969
Sample C	500	218.09	0.9995
Sample D	1000	218.02	0.9936
Sample E	1500	218.19	0.9955
Sample F	3000	217.55	0.9957

6.4 Comparison of Different Monitoring Techniques

On the specimen used in this work several measurements techniques were applied. Consequently, measurements of hardness, Young's modulus, classical quadratic nonlinearity β and non-classical hysteretic nonlinearity α can be compared in their ability to monitor microstructural changes. Figure 6.3 compares the results of the Rockwell C hardness, Young's modulus, β and α measurements. To be able to compare these results, the values are normalized to their initial state (0 h heat treatment). The errorbars represent the highest and lowest result for the β and hardness measurements. The variability of α and the Young's modulus is implied by indicating $\pm 2\sigma$ with the error bars and thus representing approximately 95 % of the realizations. The figure reveals that hardness and Young's modulus are much less sensitive to microstructural changes than measurements of nonlinear parameters. Furthermore, the hardness fails to monitor changes after 500 hours heat treatment. The changes until 500 hours heat treatment are represented by a 45 % decrease in $|\alpha|$ and a 30 %, 12 % and 0.5 % change in β, hardness and Young's modulus, respectively. After 500 hours holding time, the hardness only exhibits small changes while the nonlinear measurements α and β change by around 80 % and 60 %, respectively. The fact that the slope of α

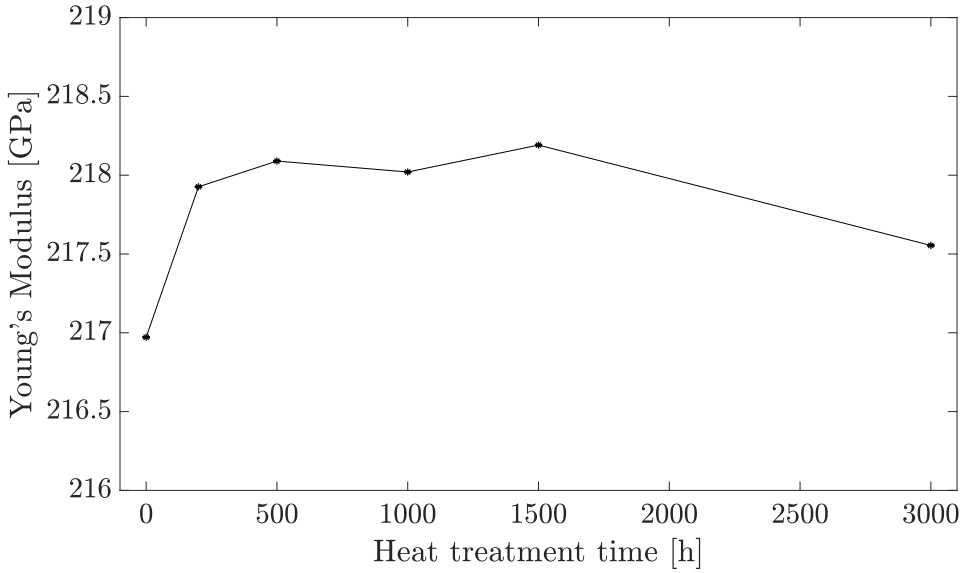

Figure 6.2: Young's Modulus of the Cr9Mo1 specimen plotted over heat treatment time. The errorbars indicate $\pm 2\sigma$.

and β even changes the sign indicates that one microstructural effect is dominantly influencing the nonlinear parameters in the beginning, while another effect causes the increase after 500 hours heat treatment. In opposition to that, for example the hardness continuously decreases logarithmically over all heat treatments done in this experiment. Marino et al. [21] divides the heat treatment in two phases: An initial phase which leads to decreasing β followed by a second phase which is indicated by increasing β. The initial phase shows a simultaneous decrease in hardness and β. Marino et al. concludes that this decrease in β up to 500 hours is mainly caused by the reduction of dislocation density. In the second phase, the growth of precipitated particles dominates the influences on the quadratic nonlinearity parameter β and causes an increase which, at a holding time of 3000 hours, even exceeds the initial nonlinearity by 13 %. In the second phase, the influence of decreasing dislocation density is comparably small and thus does not dominantly influence the β nonlinearity.

Interestingly, the non-classical hysteretic nonlinearity follows the exact same pattern, despite the higher significance. The behavior of α can also be separated in an

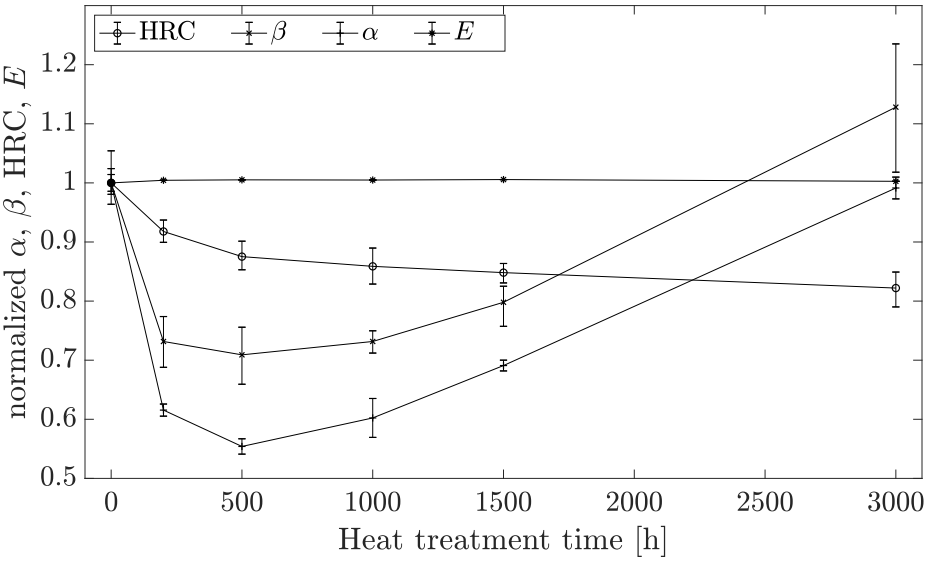

Figure 6.3: Results for α, β, Rockwell C hardness and Young's modulus at the Cr9Mo1 specimen, plotted over heat treatment time. All data series are normalized to the value of the initial state.

initial phase up to 500 hours holding time and a second phase. The dislocation pinning model by Granato and Lücke [12] described in chapter 2 gives an explanation for the decrease of α in the initial phase. When the dislocation density decreases, clearly the described effect is weakened and the overall hysteretic nonlinearity lowers. Figure 6.4 gives an overview over the microstructural processes that develop over the course of the heat treatment of Cr9Mo1 together with the measurement results.

6.5 Comparison with Results from 17-4PH Stainless Steel

The precipitation hardening steel 17-4PH was examined by Thiele et al. [28], Matlack et al. [29] and Maier et al. [9] and the results are presented here to further examine how the nonlinear parameters α and β react on microstructural changes.

17-4PH stainless steel is known to harden through the formation of copper precipitates during thermal aging until peak aging time [30]. The thermal aging of 17-4PH is examined at four specimen with increasing thermal aging time at $400°C$. This temperature was chosen low enough so that the dislocation density approximately

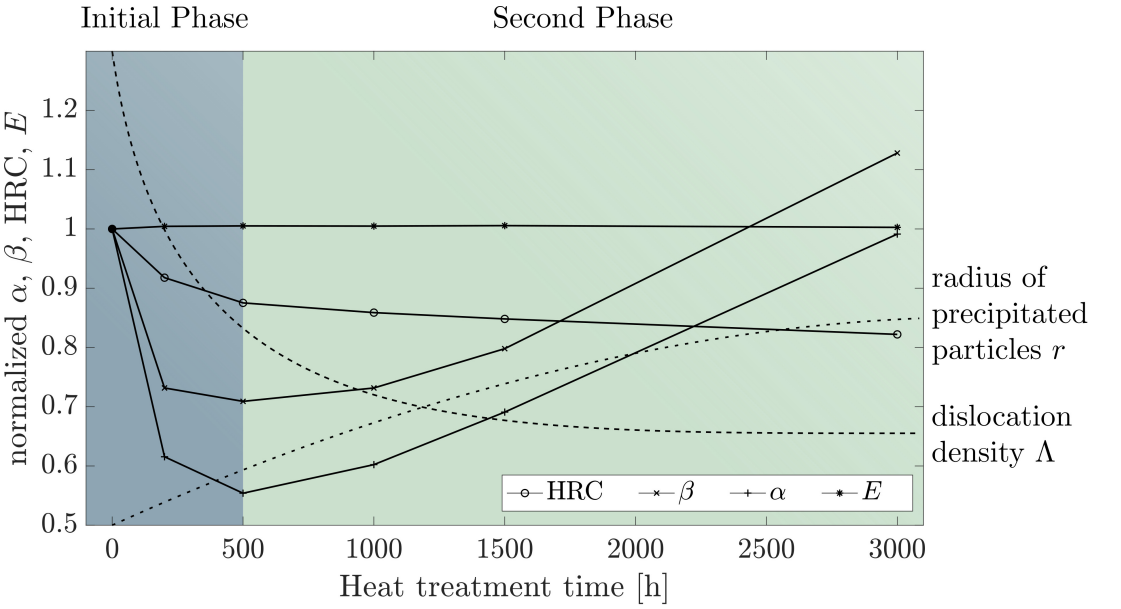

Figure 6.4: Overview over the microstructural processes that develop over the course of the heat treatment of Cr9Mo1 together with the measurement results.

remained constant [29]. All samples were solution annealed at 1050°C for six hours beforehand, ensuring that the samples initially showed no copper precipitates [1]. Thermal aging at temperatures of 400°C and higher hardens the material [31]. On these specimen hardness, Young's modulus, β and α measurements were performed. Figure 6.5 shows a comparison of the results, displayed normalized to the initial state.

Because the heat treatment is thought to not influence the dislocation density in this material, it is compared to the second phase of the heat treatment of the Cr9Mo1 specimen where the dislocation density is also not changing significantly. The absolute hysteretic nonlinearity $|\alpha|$ is rising over both of these heat treatments. While the hardness is more or less constant for Cr9Mo1, it increases significantly at 17-4PH. However, the classical quadratic nonlinear parameter β shows an opposite trend for the two materials. It is increasing during the second phase of the heat treatment applied to Cr9Mo1 while it decreases for 17-4PH. This contrary behavior of α and β highlights that these two nonlinearities rely on separated microstructural effects which are only indirectly correlated through, for example, the dislocation density. Matlack

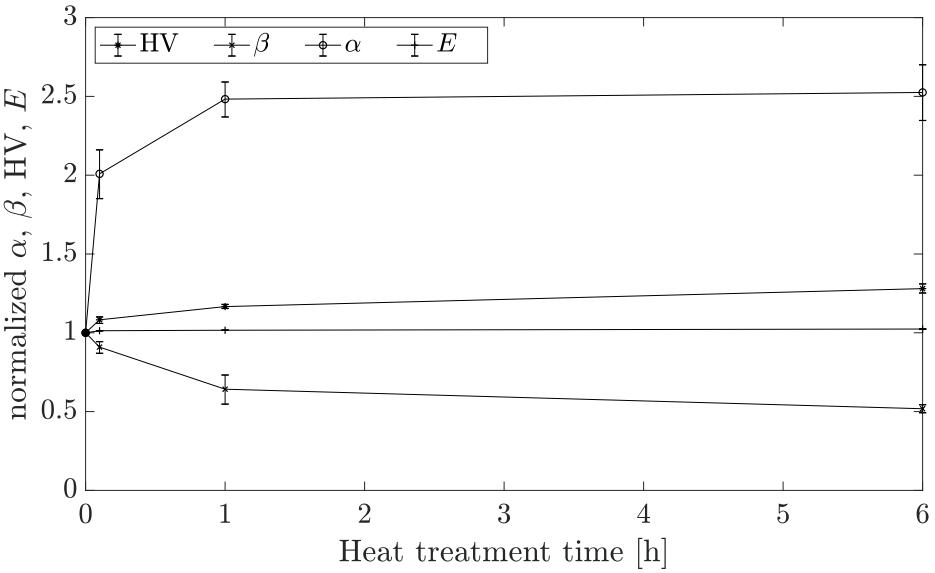

Figure 6.5: Results for α, β, Vickers hardness and Young's modulus at the 17-4PH specimen, plotted over heat treatment time. All data series are normalized to the value of the initial state.

et al. [29] state, based on [32], that the change of β is related to the dislocation density Λ, the average radius of the precipitates r and the number density of the precipitates N as follows:

$$\Delta\beta \propto \frac{\Lambda r^3}{N^{\frac{1}{3}}}. \tag{6.1}$$

Furthermore, Matlack et al. [29] say that the radius of the precipitates is roughly constant over the heat treatment and thus the decrease of β is due to the nucleation of precipitates (increase of N). In opposition to that, Marino et al. [21] state a growth of precipitated particles in the second phase of the heat treatment. This could explain a rising β when the number density of the precipitates N is not significantly increasing at the same time. Therefore, equation (6.1) could explain the trend of β in both materials.

The heat treatments on both materials have in common that the volume fraction of the precipitates is increasing. On a mesoscopic level, hysteresis is due to soft regions bonding together hard aggregate, like precipitates [33]. This could explain the rising

absolute value of α. However, more investigation has to be done to fully understand the reaction of α to mircostructural changes.

CHAPTER 7
CONCLUSION AND OUTLOOK

7.1 Conclusion

The NRUS experimental setup developed by Maier et al. [1] was successfully applied and could be improved in several aspects. The positioning with four screws ensures precise positioning relative to the exciting transducer and the laser vibrometer. A longer excitation sequence enables longer measurements without disturbance and gradually increasing and decreasing the excitation amplitude naturally cancels out environmental influences. Furthermore, the post-processing has been improved and is now more robust against possible environmental influences. Giving special attention to the alignment of the two reflecting surfaces of the specimen was detected to be essential to get consistent strain amplitudes throughout every sample.

With an added temperature measurement next to the specimen, the dominant influence of temperature on the NRUS measurement could be found. First, a formula for the influence of the temperature due to Young's modulus changes could be theoretically derived and then this model was validated with acquired temperature data.

In this study, NRUS measurements were applied on Cr9Mo1 samples. The results for the hysteretic nonlinearity parameter α showed the same trend as previously conducted β measurements. Although, the hysteretic nonlinearity α is more sensitive to microstructural changes.

The resulting values for α and β, measured on the Cr9Mo1 samples, are in agreement to each other in a sense that they change from specimen to specimen with the same direction. However, other research reports a diverging of the two nonlinearity

parameters which can be explained by the different mircostructural effects causing each nonlinearity.

7.2 Outlook

The disconnected behavior of α and β has to be examined in further studies. These two sets of measurements can give decisive hints how α reacts on microstructural changes. Besides that, the fact that α and β react differently implies that a measurement of both nonlinearity parameters can give further insight about the microstructure than one measurement alone.

In this study it has been shown that the resonance measurement is highly sensitive to to both the strain amplitude and the temperature. To account for ambient temperature changes, a correction procedure based on Haupert et al. [6] was applied. Although this method works very well and leads to good results, the dependency on two physical quantities is suited for a multiple linear regression. From the theory done in chapter 2 and 4 equation (2.3) and (5.7) give the (empirical) dependence of the frequency to the strain amplitude

$$\frac{\Delta f}{f_0} = \alpha\hat{\varepsilon} \quad \Leftrightarrow \quad f_n \propto \hat{\varepsilon} + c \tag{7.1}$$

with some constant c and to the temperature

$$f_n^2 \propto T + b \tag{7.2}$$

with some constant b. This leads to the combined equation

$$f_n^2 = a_0 + a_1 T + a_2 \hat{\varepsilon}^2 + a_3 \hat{\varepsilon}. \tag{7.3}$$

with constants a_0, a_1, a_2 and a_3. With a multiple linear regression these constants

can be determined in a way that the gathered data is best represented. The constants a_2 and a_3 result with a completion of the square to the y-intercept and slope defining the linear relationship in equation (7.1). The residual of a_0 and a_1 lead to the linear relationship between Young's modulus and the temperature ((5.7)). This technique could further simplify the measurement procedure and would make the measurements at reference excitation amplitude obsolete. Therefore, the overall process would only take half the time.

REFERENCES

[1] S. Maier, J.-Y. Kim, M. Forstenhäusler, J. J. Wall, and L. J. Jacobs, "Non-contact nonlinear resonance ultrasound spectroscopy (nrus) for small metallic specimens," *NDT & E International*, vol. 98, pp. 37–44, 2018.

[2] B. Arivazhagan, R. Prabhu, S. Albert, M. Kamaraj, and S. Sundaresan, "Microstructure and mechanical properties of 9cr-1mo steel weld fusion zones as a function of weld metal composition," *Journal of materials engineering and performance*, vol. 18, no. 8, p. 999, 2009.

[3] J. Hald, "Microstructure and long-term creep properties of 9–12% cr steels," *International Journal of Pressure Vessels and Piping*, vol. 85, no. 1-2, pp. 30–37, 2008.

[4] K. E. A. Van Den Abeele, P. A. Johnson, and A. Sutin, "Nonlinear elastic wave spectroscopy (NEWS) techniques to discern material damage. Part I: Nonlinear wave modulation spectroscopy (NWMS)," *Research in Nondestructive Evaluation*, vol. 12, no. 1, pp. 17–30, 2000.

[5] K. Matlack, J.-Y. Kim, L. Jacobs, and J. Qu, "Review of second harmonic generation measurement techniques for material state determination in metals," *Journal of Nondestructive Evaluation*, vol. 34, no. 1, p. 273, 2015.

[6] S. Haupert, G. Renaud, J. Riviere, M. Talmant, P. A. Johnson, and P. Laugier, "High-accuracy acoustic detection of nonclassical component of material nonlinearity," *The Journal of the Acoustical Society of America*, vol. 130, no. 5, pp. 2654–2661, 2011.

[7] K. H. Matlack, "Nonlinear ultrasound for radiation damage detection," PhD thesis, Georgia Institute of Technology, 2014.

[8] K.-A. Van Den Abeele, J. Carmeliet, J. A. Ten Cate, and P. A. Johnson, "Nonlinear elastic wave spectroscopy (news) techniques to discern material damage, part ii: Single-mode nonlinear resonance acoustic spectroscopy," *Journal of Research in Nondestructive Evaluation*, vol. 12, no. 1, pp. 31–42, 2000.

[9] S. G. Maier, "Noncontact nonlinear resonance ultrasound spectroscopy for small metallic samples," PhD thesis, Georgia Institute of Technology, 2017.

[10] I. Mayergoyz, "Hysteresis models from the mathematical and control theory points of view," *Journal of Applied Physics*, vol. 57, no. 8, pp. 3803–3805, 1985.

[11] R. A. Guyer and P. A. Johnson, "Nonlinear mesoscopic elasticity: Evidence for a new class of materials," *Physics today*, vol. 52, pp. 30–36, 1999.

[12] A. v. Granato and K. Lücke, "Theory of mechanical damping due to dislocations," *Journal of applied physics*, vol. 27, no. 6, pp. 583–593, 1956.

[13] K.-Y. Jhang, "Nonlinear ultrasonic techniques for nondestructive assessment of micro damage in material: A review," *International journal of precision engineering and manufacturing*, vol. 10, no. 1, pp. 123–135, 2009.

[14] J. Chen, J.-Y. Kim, K. E. Kurtis, and L. J. Jacobs, "Theoretical and experimental study of the nonlinear resonance vibration of cementitious materials with an application to damage characterization," *The Journal of the Acoustical Society of America*, vol. 130, no. 5, pp. 2728–2737, 2011.

[15] T. Ohtani, Y. Kusanagi, and Y. Ishii, "Noncontact nonlinear resonant ultrasound spectroscopy to evaluate creep damage in an austenitic stainless steel," in *AIP Conference Proceedings*, AIP, vol. 1511, 2013, pp. 1227–1233.

[16] C. Payan, T. J. Ulrich, P.-Y. Le Bas, T. Saleh, and M. Guimaraes, "Quantitative linear and nonlinear resonance inspection techniques and analysis for material characterization: Application to concrete thermal damage," *The Journal of the Acoustical Society of America*, vol. 136, no. 2, pp. 537–546, 2014.

[17] J. F. Gregg and B. E. Anderson, "Nonlinear resonant ultrasound spectroscopy using electromagnetic excitation," *The Journal of the Acoustical Society of America*, vol. 145, no. 3, pp. 1925–1925, 2019.

[18] L. E. Kinsler, A. R. Frey, A. B. Coppens, and J. V. Sanders, "Fundamentals of acoustics," *Fundamentals of Acoustics, 4th Edition, by Lawrence E. Kinsler, Austin R. Frey, Alan B. Coppens, James V. Sanders*, p. 560, Dec. 1999.

[19] H. K. Danielsen, "Z-phase in 9-12% cr steels," PhD thesis, Technical University of Denmark (DTU), 2007.

[20] P. D. Jablonski, D. Alman, O. Dogan, G. Holcomb, and C. Cowen, "9 cr–1 mo steel material for high temperature application," National Energy Technology Lab.(NETL), Pittsburgh, PA, and Morgantown, WV ..., Tech. Rep., 2012.

[21] D. Marino, J.-Y. Kim, A. Ruiz, Y.-S. Joo, J. Qu, and L. J. Jacobs, "Using nonlinear ultrasound to track microstructural changes due to thermal aging in modified 9% cr ferritic martensitic steel," *NDT & E International*, vol. 79, pp. 46–52, 2016.

[22] J. Pešička, R. Kužel, A. Dronhofer, and G. Eggeler, "The evolution of dislocation density during heat treatment and creep of tempered martensite ferritic steels," *Acta materialia*, vol. 51, no. 16, pp. 4847–4862, 2003.

[23] W. B. Jones, C. Hills, and D. Polonis, "Microstructural evolution of modified 9cr-1mo steel," *Metallurgical Transactions A*, vol. 22, no. 5, pp. 1049–1058, 1991.

[24] *1040l broadband power amplifier*, Revision F, Electronics & Innovation, Dec. 2012.

[25] *Ntc thermistors, standard lug sensors*, 29092, Vishay BCcomponents, Oct. 2018.

[26] H. Ledbetter, "Stainless-steel elastic constants at low temperatures," *Journal of Applied Physics*, vol. 52, no. 3, pp. 1587–1589, 1981.

[27] E. Garofalo, P. Malenock, and G. Smith, "The influence of temperature on the elastic constants of some commercial steels," *Determination of Elastic Constants, Special Technical Publication, American Society for Testing and Materials*, p. 10, 1952.

[28] S. Thiele, "Air-coupled detections of rayleigh surface waves to assess material nonlinearity due to precipitation in alloy steel," Master's thesis, Georgia Institute of Technology, Atlanta, GA, USA, Aug. 2013.

[29] K. H. Matlack, H. A. Bradley, S. Thiele, J.-Y. Kim, J. J. Wall, H. J. Jung, J. Qu, and L. J. Jacobs, "Nonlinear ultrasonic characterization of precipitation in 17-4ph stainless steel," *NDT & E International*, vol. 71, pp. 8–15, 2015.

[30] M. Murayama, K. Hono, and Y. Katayama, "Microstructural evolution in a 17-4 ph stainless steel after aging at 400 c," *Metallurgical and Materials Transactions A*, vol. 30, no. 2, pp. 345–353, 1999.

[31] H. Mirzadeh and A. Najafizadeh, "Aging kinetics of 17-4 ph stainless steel," *Materials chemistry and physics*, vol. 116, no. 1, pp. 119–124, 2009.

[32] J. H. Cantrell and W. T. Yost, "Determination of precipitate nucleation and growth rates from ultrasonic harmonic generation," *Applied Physics Letters*, vol. 77, no. 13, pp. 1952–1954, 2000.

[33] M. W. Barsoum, M. Radovic, T. Zhen, P. Finkel, and S. R. Kalidindi, "Dynamic elastic hysteretic solids and dislocations," *Physical review letters*, vol. 94, no. 8, p. 085 501, 2005.